Western Graduate&PostdoctoralStudies

Western University
Scholarship@Western

Electronic Thesis and Dissertation Repository

6-16-2014 12:00 AM

A Non-Contrast Magnetic Resonance Imaging Technique to Assess Blood-Brain Barrier Permeability

Harini Pandithasekera, *The University of Western Ontario*

Supervisor: Dr. Keith St. Lawrence, *The University of Western Ontario*

A thesis submitted in partial fulfillment of the requirements for the Master of Science degree in Medical Biophysics

© Harini Pandithasekera 2014

Follow this and additional works at: https://ir.lib.uwo.ca/etd

Part of the Biological and Chemical Physics Commons, Medical Biophysics Commons, and the Neuroscience and Neurobiology Commons

Recommended Citation

Pandithasekera, Harini, "A Non-Contrast Magnetic Resonance Imaging Technique to Assess Blood-Brain Barrier Permeability" (2014). *Electronic Thesis and Dissertation Repository*. 2152.
https://ir.lib.uwo.ca/etd/2152

This Dissertation/Thesis is brought to you for free and open access by Scholarship@Western. It has been accepted for inclusion in Electronic Thesis and Dissertation Repository by an authorized administrator of Scholarship@Western. For more information, please contact wlswadmin@uwo.ca.

A NON-CONTRAST MAGNETIC RESONANCE IMAGING TECHNIQUE TO ASSESS BLOOD-BRAIN BARRIER PERMEABILITY

(Thesis format: Monograph)

by

Harini Pandithasekera

Graduate Program in Medical Biophysics

A thesis submitted in partial fulfillment
of the requirements for the degree of
Masters of Science

The School of Graduate and Postdoctoral Studies
The University of Western Ontario
London, Ontario, Canada

© Harini Pandithasekera 2014

Abstract

The Blood-brain barrier (BBB) regulates the entry of compounds between the blood and the brain, thus plays an important role in brain homeostasis. Studies indicate in disease states such as Alzheimer's the BBB integrity is compromised. The motive of this project is to investigate the sensitivity of the diffusion-weighted arterial spin labeling (DW-ASL) technique to detect water exchange. Testing the sensitivity requires a reliable method of opening the barrier at specific locations of the brain. Here, a unique technology named focused ultrasound (FUS) has been used to mimic a compromised BBB environment.

A series of experiments were conducted in a piglet model to determine the ideal settings for a successful BBB opening. The combination of 2.5 W of power, 0.02 ml/kg of microbubble concentration while saturated O_2 levels in the piglet were controlled revealed the most effective BBB opening without causing hemorrhage. Although the study was able to show a significant BBB opening in contrast-enhanced MRI, the DW-ASL images showed no significant difference between the sonicated and non-sonicated ROIs. However, the average water exchange rate (k_w) of 106 min^{-1} measured in this study corresponds to a permeability surface area product (PS_w) of 159 ml/100 g/min, which was comparable to the measurements in the prior study involving humans.

Keywords

Blood-Brain Barrier, Arterial Spin Labeling, Magnetic Resonance Imaging, Pseudo-Continuous Arterial Spin Labeling, Focused Ultrasound, Microbubbles, Blood-Brain Barrier Disruption, Piglet, Porcine, Water Exchange Rate, Permeability Surface Area Product of Water, Arterial Transit Time, Tissue Transit Time

Acknowledgments

I owe my deepest gratitude to my supervisor Dr. Keith St. Lawrence who has been guiding, supporting and encouraging me since I started working on my masters. I have a lot to learn from Dr. St. Lawrence, his patience, optimism and passion for science is truly remarkable and inspiring to us all.

I would also like to acknowledge and thank my advisory committee Dr. Rob Bartha and Dr. Neil Gelman for their time, advice and constructive feedback on the research work that I did. Without your input, this truly wouldn't be what it stands today.

Thank you to Dr. Ting Yim-Lee for letting me use the Focused Ultrasound machine for my experiments and his student Hassaan Ahmed for the early training on the machine.

To the wonderful ladies at the lab, Jennifer Hadway, Laura Morrison and Lise Desjardins, I would not be able to collect a single set of data without you all. Thank you for being ever so patient, sitting through painstaking 8-hour experiments. I would specially like to mention Jenn's dedication to get this complicated experiment rolling. I would like to say a special thanks to John Butler for teaching me how to safely run the MRI scanner by myself. You taught me invaluable little tricks, helping me set up the MRI protocols as well as trouble shoot many of the little issues that I faced along the way.

I would like to thank my lab mate Udunna Anazodo, for her input (you are an absolute genius!), SPM tutorials, constant jokes, coffee and venting sessions. I am also grateful for my office mates Karina, Reggie, Anindita and Lin Shan for the frequent chats and good times during the break, helping each other keep sane!

To my best friends, Senuri and Tasha, thank you for the regular chats on life, all-you-can-eat sushi, cooking sessions, sleep overs, London - Toronto drives, and of course for keeping tabs on me!

I am forever in debt to my parents for their unconditional love and support through my academic endeavors and for always believing in my pursuit of a higher education.

Finally, to my amazing fiancé Rasike for always being there for me, lifting my spirits, spoiling me, making me laugh and just simply being my other half through this journey. I couldn't imagine a better person to spend the rest of my life with.

Table of Contents

Abstract ..... **ii**

Acknowledgments ..... **iii**

Table of Contents ..... **v**

List of Tables ..... **vii**

List of Figures ..... **viii**

List of Appendices ..... **xi**

List of Abbreviations ..... **xii**

Chapter 1 ..... **1**

1 Introduction **1**

1.1 The Blood-Brain Barrier 1

1.1.1 Transport of Water through the Blood-Brain Barrier *3*

1.1.2 Blood-Brain Barrier Dysfunction and its Possible Role in Neurovascular Disease *5*

1.2 Arterial Spin Labeling 7

1.2.1 Continuous Arterial Spin Labeling *8*

1.3 Quantification Issues in ASL 13

1.4 Assessing Water Exchange Across the BBB by ASL 15

1.5 Opening the Blood-Brain Barrier 23

1.6 Introduction to Focused Ultrasound 24

1.6.1 Mechanisms for Blood-Brain Barrier Disruption: Acoustic Cavitation and Radiation Pressure *25*

1.6.2 The Role of Microbubbles in Focused Ultrasound *26*

1.6.3 The Effect of Acoustic Parameters of Ultrasound *28*

1.6.4 Challenges to Disrupting the Blood-Brain Barrier by Focused Ultrasound *29*

1.7 Porcine Studies to Date 31

1.8 Objectives, Rationale and Overview of the Project 33

Chapter 2 ..... **34**

2 Materials and Methods **34**

2.1 Animal Preparation 34

2.2 Experimental Procedure 35

2.2.1 Sonication Protocol *35*

2.2.2 Permeability Imaging Protocol *38*

2.2.3 Optimization of the FUS Power *41*

2.3 Data Analysis 41

2.4 Statistics and Sensitivity Analysis 43

Chapter 3 ..... **44**

3 Results **44**

3.1 Optimization of the FUS Power 44

3.2 DW-ASL Results 48

Chapter 4 ..... **53**

4 Discussion **53**

Chapter 5 ..... **59**

5 Summary **59**

5.1 Limitations and Future Work 59

5.2 Conclusion 60

References **61**

Appendices **72**

Curriculum Vitae **74**

List of Tables

Table 3.1: T_2^* values of the sonicated and non-sonicated regions for all power groups 48

Table 3.2: Whole-brain average tissue transit time (τ_b) and water exchange rate (k_w).....49

Table 3.4: Mean pixel SNR in the FEAST and DW-ASL image sets. 52

Table 3.3: Calculated water exchange rate (k_w) for the sonicated and non-sonicated regions for all 6 piglets. 52

List of Figures

Figure 1.1: The neurovascular unit. Adapted from Fisher, M. 2009 (3). 1

Figure 1.2: Various methods of molecule transport across the BBB. Adapted from Re, F *et al*., 2012 (6) 3

Figure 1.3: The difference between the muscle capillary endothelium and the brain capillary endothelium (BBB). The lack of pores and slits in the BBB hinders bulk flow of water..... 4

Figure 1.4: The white lines depict the imaging slice. (a) Continuous adiabatic inversion (red line) is applied proximally to the imaging slice. (b) An off - resonance pulse (red line) is applied distally to the imaging slice to correct for magnetization transfer (MT) effects. (c) Double inversion of arterial spins using amplitude- modulated CASL for multislice ASL imaging..... 9

Figure 1.5: The two-compartment model for CASL consisting of the arterial and tissue compartments. The time it takes labeled blood to reach the arterial compartment is the arterial transit time (τ_a), and the time it takes for labeled blood to reach the tissue compartment is the tissue transit time (τ_b).....14

Figure 1.6: Capillary – Tissue Exchange Model. The BBB separates the two compartments. $M_c(t)$ and $M_b(t)$ represent the magnetization in the capillary and brain tissue spaces.....16

Figure 1.7: (A) Before and (B) administrating an osmotic agent. Injection of The hyperosmolar osmotic reagents leads to shrinking of the endothelial cells and subsequently enlarges the pore size by opening the TJs. Adapted from Rebeles, F *et al*., 2006 (52) 23

Figure 1.8: Possible mechanisms for BBBD via FUS and MBs: TJ separation by radiation force, bubble oscillation or by acoustic streaming. Adapted from Vykhodtseva, N *et al*., 2008 (62) 25

Figure 2.1: Left: The monitor that displays the GUI. Middle: The FUS system that is filled with degassed water. Right: The electronics cart consisting of the controls and power supply. (*Images from http://www.fusinstruments.com*) 35

Figure 2.2: Location of the axial T_1-weighted images, which was defined using landmarks identified in the sagittal images. 36

Figure 2.3: Schematic diagram of the FUS set up during sonication. Right: MR image showing the location of six targeted points. 37

Figure 2.4: The DW-ASL sequence is a modification of the standard pCASL technique. DW-ASL consists of pCASL with a twice-refocused spin-echo diffusion imaging sequence. Adapted from St. Lawrence *et al*., (47).....39

Figure 3.1: T_1 and T_2^*-weighted images at the three sonication powers. Row 1: Post Gd-DTPA T_1 images, Row 2: T_2^*-weighted images. The yellow arrows indicate the BBB opening while the orange arrows indicate the hemorrhage at the ventricles 45

Figure 3.2: Ratio of the signal intensity from the post Gd-DTPA T_1-weighted images from the sonicated ROI to the non-sonicated ROI plotted as the FUS power. Asterisks indicate significant signal increase between the two ROIs. 45

Figure 3.3: Histology with Evans Blue dye seen on tissue sections that corresponded to the targeted FUS slices. 46

Figure 3.4: Signal decay curves from the T_2^*-weighted images at 2.5 W (sonicated and non-sonicated ROIs) and 6 W (sonicated ROI). The 2.5 W data were averaged over 6 animals; whereas, the 6.0 W data were acquired from one animal. 47

Figure 3.5: a) Sonicated ROI as shown on the post Gd-DTPA T_1-weighted image. b) Corresponding co-registered b = 50 s/mm^2 DW-ASL image. c) The fusion of the DW-ASL and the T_1-weighted images to demonstrate the overlap.

The coregistration image is produced using MRIcron (Neuroimaging Tools and Resources, McCausland Center for Brain Imaging, SC, USA). 49

Figure 3.6: FEAST and DW-ASL data from one piglet: (a) FEAST data acquired with a PLD = 500 ms and (b) DW-ASL data acquired with a PLD = 1000 ms. Each data set shows the average diffusion-weighted ΔM_{b_0} in the first row and $\Delta M_{b_{DW}}$ in the second row. The ratio image, $\Delta M_{b_{DW}}/\Delta M_{b_0}$ is shown in the third row. The b values for FEAST and DW-ASL were 10 and 50 s/mm^2, respectively. All images have been first masked to show only the brain and smoothed with a 7 mm Gaussian filter.....51

Figure 4.1: Predicted capillary fraction of labeled water (A_1) plotted as a function of the water-exchange rate (k_w). These simulated data were generated using T_{1b} = 1.26 s, T_{1a} = 1.49 s, a labeling duration of 1.5 s, τ_b = 1.06 s and a PLD of 1.0 s. .55

List of Appendices

Appendix A: Animal Protocols 72

List of Abbreviations

α	$Model\ Parameter = (PS/V_c) + R_{1a}$
A_1	Predicted Capillary Fraction of Labeled Water
A_2	Tissue Fraction of Labeled Water
AD	Alzheimer's Disease
AFP	Adiabatic Full Passage
AQP4	Aquaporin-4
ASL	Arterial Spin Labeling
Aβ	Amyloid Beta Peptides
β	$Model\ Parameter = 1/(1 + (\Delta R_1 V_c/PS))$
b	Diffusion Gradient Strength (s/mm^2)
b_0	Diffusion Gradient Strength = 0 s/mm^2
b_{DW}	Applied Diffusion Gradient Strength (s/mm^2)
BBB	Blood-Brain Barrier
BBBD/BBBDs	Blood-Brain Barrier Disruption (s)
BM	Basal Membrane
CASL	Continuous Arterial Spin Labeling
CBF	Cerebral Blood Flow
CNS	Central Nervous System
CSF	Cerebral Spinal Fluid
Δ_{label}	Duration of the Labeling Pulse
D_1	Apparent Diffusion Coefficient of the Labeled Capillary Water

D_2	Apparent Diffusion Coefficient of the Tissue Labeled Water
DW-ASL	Diffusion- Weighted Arterial Spin Labeling
EB	Evans Blue
EC	Endothelial Cells
ECM	Endothelial Cell Membrane
EPI	Echo Planar Imaging
ε	Labeling / Tagging Efficiency
F	Cerebral Blood Flow
FEAST	Flow-Encoding Arterial Spin Tagging
FOV	Field-of-View
FUS	Focused Ultrasound
γ	Gyromagnetic Ratio of Protons
G	Gradient Strength
Gd-DTPA	Gadolinimum-diethylenetriaminepentaacetic acid
GLUT1	Glucose Transporter
GRAPPA	Generalized Autocalibrating Partially Parallel Acquisition
H_1	Radiofrequency Magnetic Field Strength
k_w	Water Exchange Rate
λ	Blood/Tissue Partition Coefficient of Water (0.9 g/ml)
LAT1	Large Neutral Amino Acid Transporter
LRP	Lipoprotein Receptor elated Protein - 1 receptor
M_a^C	Arterial Magnetization for the Control Condition

M_a^L	Arterial Magnetization for the Labeled Condition
M_b^0	Equilibrium Magnetization of Tissue
M_b	Tissue Magnetization
M_c	Capillary Magnetization
$\Delta\mathrm{M}_a$	ASL Signal in the Arterial Compartment
ΔM_b^0	Equilibrium Magnetization of Tissue
$\Delta\mathrm{M}_b$	ASL Signal in the Tissue/Capillary Compartment
$\Delta\mathrm{M}_c$	ASL Signal within the Capillaries
ΔM	ASL Signal (Control – Tag)
$\Delta M\ (t, 0)$	ASL Signal While No Diffusion Gradient was applied
$\Delta M\ (t, b)$	ASL Signal during the Application of the Diffusion Gradient
MB/MBs	Microbubble (s)
MRI	Magnetic Resonance Imaging
MT	Magnetization Transfer
OFP	Octafluoropropane
$PaCO_2$	Partial Pressure of CO_2
PaO_2	Partial Pressure of O_2
PASL	Pulsed Arterial Spin Labeling
pCASL	Pseudo-Continuous Arterial Spin Labeling
PESDA	Perfluorocarbon-Exposed Sonicated Dextrose albumin
PET	Positron Emission Tomography
PLD	Post Labeling Delay

PRF	Pulse Repetition Frequency
PS	Permeability Surface Area Product
PS_w	Capillary Permeability Surface-Area Product of Water
PVH	Periventricular Hyperinstensity
q_b	Concentration Of Labeled Water in the Tissue (Impulse Residue Function)
q_c	Concentration Of Labeled Water in the Capillary (Impulse Residue Function)
R_{1a}	Longitudinal Relaxation Rate of Blood
R_1^{RF}	Tissue Relaxation in the Presence of an Off-Resonance Pulse
RAGE	Receptor for Advanced Glycation End Products
RF	Radiofrequency
ROI	Region-of-Interest
SGL	Surface Glycocalyx Layer
SNR	Signal-to-Noise Ratio
SPECT	Single-Photon Emission Computed Tomography
τ_a	Arterial Transit Time
τ_b	Tissue Transit Time
T_1	Longitudinal Relaxation Time
T_1^a	Longitudinal Relaxation of Arterial Blood
T_2^*	Relaxation due to Magnetic Field Inhomogeneities and Susceptibility Effects
T_2	Transversal Relaxation Time due to Spin-Spin Interaction
TE	Echo Time
TJ	Tight Junctions

TR	Repetition Time
ν	Linear Velocity of the Inflowing Arterial Spins
V_c	Capillary Blood Volume (mL/100mg)
w	Post Labeling Delay
WEI	Water Exchange Index
WML	White Matter Lesions

Chapter 1

1 Introduction

1.1 The Blood-Brain Barrier

By regulating the entry of compounds from the blood into the brain, the blood-brain barrier (BBB) plays a critical role in brain homeostasis (1). The BBB consists of a series of endothelial cells (EC) that are linked with tight junctions (TJ) (Figure 1.1). The luminal membrane of the endothelial layer is covered with a surface glycocalyx layer (SGL), while the basement membrane (BM) surrounds the abluminal surface. The BM consists of extracellular matrix (ECM) proteins such as collagen (type IV), heparin sulfate proteoglycans and fibronectin. Astrocyte foot processes completely surround the tissue side of the capillary wall, holding the endothelial cells and pericytes in place (2).

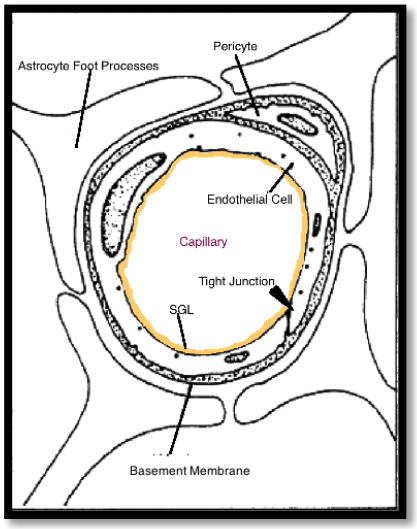

Figure 1.1: The neurovascular unit. Adapted from Fisher, M. 2009 (3).

The majority of molecules that enter the brain tissue through the BBB are small (under 400 Da) and lipophilic (4). Molecules cross the BBB by either paracellular or transcellular pathways. The paracellular pathway refers to transport through the intercellular spaces between cells, such as TJs, while the transcellular pathway refers to the movement of substances through the cells themselves. Transcellular transport consists of both active and passive forms while the paracellular transport consists of only the passive form (Figure 1.2). Passive transport requires no energy; however, it is powered by hydrostatic, electrochemical and osmotic pressure gradients. The four types of passive transport include diffusion, facilitated diffusion, filtration and osmosis. Large molecules are said to cross the BBB through the transcellular pathway, while small molecules cross the BBB via the restricted paracellular pathway namely via diffusion (2).

Hydrophilic ions (sodium, calcium and bicarbonate) and molecules, such as glucose and lactate, cannot cross the BBB by ordinary diffusion and must rely on active transporters (i.e., facilitated diffusion) to enter the brain (1,5). The BBB encompasses different types of transporters to move compounds from blood to brain: the glucose transporter (GLUT1) for transport of glucose, large neutral amino acid transporter (LAT1) for shuttling amino acids, and P-glycoprotein and organic anion transporters to clear waste products from the brain tissue (5). Na^+-K^+-ATPase pumps, which are situated in the abluminal layer of the BBB, transport sodium and potassium ions between the blood and brain (5).

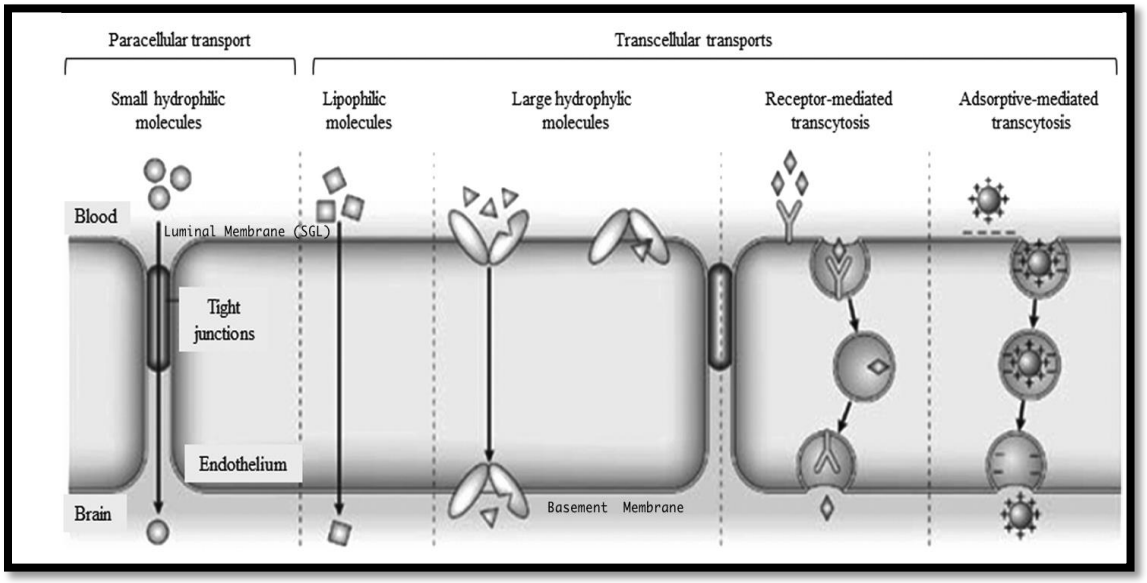

Figure 1.2: Various methods of molecule transport across the BBB. Adapted from Re, F *et al*., 2012 (6)

1.1.1 Transport of Water through the Blood-Brain Barrier

Water extravasates from the vasculature across the endothelium layers via filtration and diffusion. In the muscle capillary endothelium, water movement occurs through the slits between the cells via filtration and is 50-fold higher than water propagation via diffusion (5). However, due to the tight junctions between the EC in the BBB, water transport takes place via diffusion (Figure 1.3). The restriction of water movement across the BBB adds to the chemical stability of the microenvironment in the brain tissue (1). To further regulate water movement, the EC in the brain have very few endocytotic vesicles regulating transcellular flux. The addition of a BM and astrocyte foot processes around the endothelium also adds to the stability of the microenvironment in the central nervous system

(CNS) by lowering the permeability to water and solutes even when the TJs and the SGL are damaged by either disease or by therapeutic agents (2).

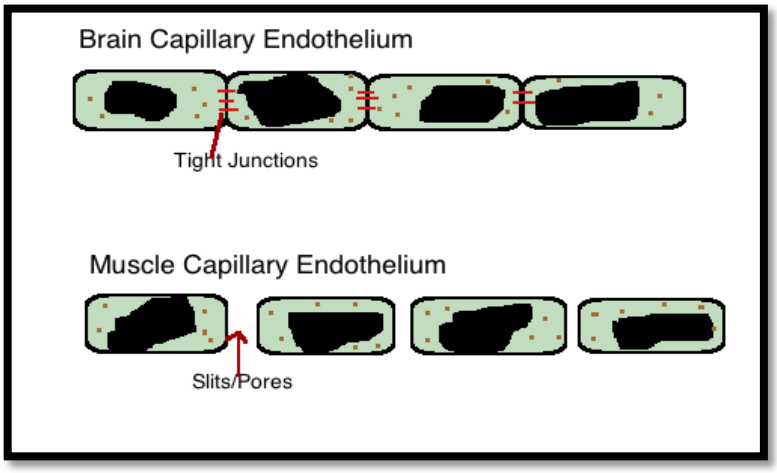

Figure 1.3: The difference between the muscle capillary endothelium and the brain capillary endothelium (BBB). The lack of pores and slits in the BBB hinders bulk flow of water

Water movement across the BBB can also occur by Aquaporin 4 (AQP4), a water-channel protein that has the ability to transfer water molecules in both directions (7). AQP4 proteins have been found to be located in astrocyte foot processes bordering the brain parenchyma and main fluid compartments like cerebral spinal fluid (CSF) and blood, indicating they are crucial for water movement in and out of the brain parenchyma (8). Research has also shown that if AQP4 proteins are removed, astrocytes have a 7-fold reduction in water permeability (7). It has also been shown using a mouse knockout model that absence of AQP4 caused water accumulation in the brain in response to ischemia, hyponatremia (Na^+ imbalance) and water poisoning (electrolyte

imbalance due to over-hydration) (7). Additionally, AQP4 deficiency contributes to brain abscesses, hydrocephalus and vasogenic edema associated with brain tumors (8).

1.1.2 Blood-Brain Barrier Dysfunction and its Possible Role in Neurovascular Disease

Alzheimer's disease (AD) is characterized by the accumulation of amyloid beta (Aβ) peptide and hyperphosphorylated tau proteins that form plaques within the brain. These block proteasome function, inhibit mitochondrial activity and alter Ca^{2+} levels, ultimately leading to neuronal loss. In addition, the accumulation of Aβ peptides and tau proteins create neurofibrillary tangles in the brain (9). The Aβ peptides while in their soluble form are transported from blood in to the brain by binding to the receptor for advanced glycation end products (RAGE), while they are cleared out of the brain by the lipoprotein receptor related protein - 1 (LRP) and P-glycoprotein, in all cases through the endothelial layer of the BBB (10–12). Research has also shown that RAGE proteins are up regulated and P-glycoprotein activity diminished with the ageing process, leading to slower clearance of Aβ peptides (10).

There is evidence that alterations in BBB permeability along with normal aging can contribute to AD progression by allowing Aβ peptides access to the brain (11,13). Inflammatory mediators such as bradykinin, seretonin and histamine increase both the BBB permeability and vessel diameter contributing to

a significant leak across the BBB (14) and may do so by altering the structure of the TJ or the transport mechanisms across the BBB (13).

Evidence of increased BBB permeability in AD patients includes the discovery of blood proteins, immune globin and albumin, in brain tissue (15). These proteins typically do not cross an intact BBB and their presence in the brain tissue suggests a compromised BBB, possibly a consequence of or a contributor to AD. In addition, a contrast-enhanced computed tomography study reported delayed washout of contrast agent, suggesting BBB dysfunction, although the results failed to reach significance (16). The loss of BBB integrity has also been reported in a transgenic mouse model of AD (17), as indicated by increased uptake of Texas red-conjugated BSA in the brain of the transgenic AD mice compared to controls.

BBB permeability can also be imaged by magnetic resonance imaging (MRI) using the contrast agent, gadolinimum-diethylenetriaminepentaacetic acid (Gd-DTPA). However, the results of contrast-enhanced MRI studies have not been consistent. Studies of AD patients and dementia patients with white matter lesions (WMLs) failed to detect a significant elevation in BBB permeability (18,19). Conversely, another study investigated the BBB permeability in WMLs in Binswanger's disease (a form of vascular dementia) and AD patients in comparison to normal WMLs in controls by assessing the periventricular hyperinstensity (PVH) in all groups (20). They reported that the BBB permeability significantly increased in areas of PVH in Binswanger's disease and AD in relation to the controls.

Detecting subtle changes in the BBB integrity associated with AD may be difficult with contrast-enhanced imaging methods because of the relatively large molecular weights of the contrast agents. (Gd-DTPA, Molecular weight = 550 Da). Consequently, BBB permeability must reach a critical level before extravasation can occur. Since water is a small solute, it has been suggested that measuring the water exchange rate may be more sensitive to subtle changes in BBB integrity that occur early in the disease process (21).

1.2 Arterial Spin Labeling

Arterial Spin Labeling (ASL) is an MRI-based technique for measuring cerebral blood flow (CBF) by using water as a flow tracer (22). Although primarily a perfusion technique, ASL can also be made sensitive to water exchange across the BBB (23) which will be described in more detail in Section 1.3. ASL measures CBF by altering the magnetization of arterial blood water flowing into the brain, causing a small reduction in the MRI signal. The application of a RF pulse inverts the net magnetization of the water in the blood. After some time (transit time) an image is acquired and that image is called a ‘labeled/tagged’ image. The image that is acquired without the inversion of the net magnetization of blood water is called a ‘control’ image. This perfusion-weighted signal (ASL signal) can be isolated by subtracting a labeled image from the control image in which the arterial blood magnetization is at equilibrium (24). The technique has been validated by comparing the perfusion measurements to established

perfusion techniques such as perfusion computed tomography (25), positron emission tomography (PET) (26), and single-photon emission computed tomography (SPECT) (27).

The two ways of tagging arterial blood water are pulsed and continuous ASL. Pulsed ASL (PASL) tags water when a single RF pulse is applied to invert the magnetization of a slab of arterial blood (28). Continuous ASL (CASL) tags water with a continuous flow-dependent adiabatic inversion of arterial blood magnetization, which is described in detail in the next section since it was the technique used in the experiments outlined in chapter 2.

1.2.1 Continuous Arterial Spin Labeling

With CASL, a constant low-power radiofrequency (RF) pulse is applied in the presence of a weak magnetic field gradient (22,29) to cause moving magnetic spins in arterial blood to experience a variation in resonance frequency, analogous to a classic adiabatic full passage (AFP) (Figure 1.4 a). For the spins to be successfully inverted under these circumstances, the 'adiabatic condition' must be met:

$$\frac{1}{T_1}, \frac{1}{T_2} \ll (1/H_1)\, G\nu \ll \gamma H_1 \tag{1.1}$$

Where, T_1 is the longitudinal relaxation time, T_2 is the transverse relaxation time, H_1 is the RF magnetic field strength, G is the gradient strength,

ν is the linear velocity of the inflowing arterial spins, and γ is the gyromagnetic ratio of protons.

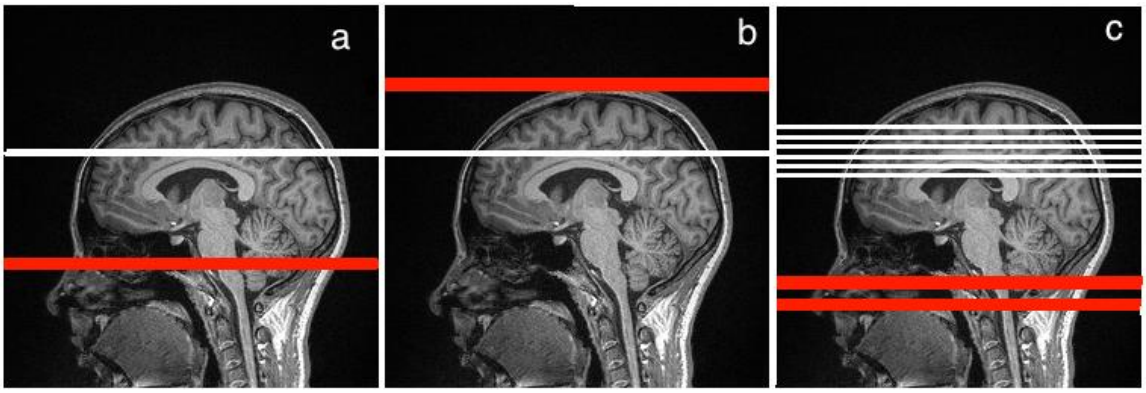

Figure 1.4: The white lines depict the imaging slice. (a) Continuous adiabatic inversion (red line) is applied proximally to the imaging slice. (b) An off - resonance pulse (red line) is applied distally to the imaging slice to correct for magnetization transfer (MT) effects. (c) Double inversion of arterial spins using amplitude- modulated CASL for multislice ASL imaging.

If the adiabatic condition is satisfied, the arterial magnetization for the labeled (M_a^L) and control (M_a^C) conditions are governed by:

$$M_a^L = \frac{M_b^0}{\boldsymbol{\lambda}} (1 - 2e^{-R_{1a}\tau_a}) \qquad R_{1a} = \frac{1}{T_{1a}} \tag{1.2}$$

$$M_a^C = \frac{M_b^0}{\boldsymbol{\lambda}} \tag{1.3}$$

where λ is the blood/tissue partition coefficient of water (0.9 g/ml), R_{1a} is the longitudinal relaxation rate of blood and M_b^0 is the equilibrium magnetization of tissue. As per the above equation, the blood magnetization is a function of equilibrium tissue magnetization because the water concentrations in the arterial space and tissue space are in equilibrium. The exponential term accounts for the arterial transit time, τ_a, which is the delay between the inversion of the arterial magnetization (labeling) and its arrival at the imaging slice (arterial compartment). Then the ASL signal in the arterial compartment is given by:

$$\Delta M_a(t) = \begin{cases} 0 & 0 < t < \tau_a \\ \dfrac{-2\varepsilon M_b^0}{\lambda} e^{-R_{1a}\tau_a} & \tau_a \leq t \leq \Delta_{label} + \tau_a \\ 0 & \Delta_{label} + \tau_a < t \end{cases} \quad (1.4)$$

where, Δ_{label} is the duration of the labeling period and ε is the labeling efficiency which accounts for the fraction of spins that were inverted. A number of factors such as RF field, relaxation effects and variations in blood velocities reduce the labeling efficiency (30)

A potential source of error with CASL is the labeling RF field causes off-resonance saturation in the imaging slice due to magnetization transfer (MT) effects. The perturbation of tissue macromolecules in the imaging slice causes signal changes that are significantly larger than the signal due to the inflow of labeled blood and, therefore, must be corrected for. A simpler way of avoiding MT effects is to apply an off-resonance pulse distally to the imaging slice during the acquisition of the control image (Figure 1.4 b). This off-resonance pulse causes the same MT effect as the labeling pulse but has no effect on the arterial spins. The disadvantage is that only one image can be acquired at a time because MT effects are managed at an equidistant from the label and control planes. The change in magnetization due to the continuous labeling of arterial blood is given by:

$$\frac{\Delta M_b(t)}{\Delta M_b^0} = \begin{cases} 0 & 0 < t < \tau_a \\ \dfrac{-2\varepsilon F}{\lambda R_1^{RF}}\, e^{-R_{1a}\tau_a}\left\{1 - e^{R_1^{RF}[t-\tau_a]}\right\} & \tau_a \le t \le \Delta_{label} + \tau_a \end{cases} \tag{1.5}$$

where, R_1^{RF} is the tissue relaxation in the presence of a off - resonance RF pulse and F is the cerebral blood flow (mL/100 g/min). If the labeling period is ideally long, the delivery of labeled blood and the rapid loss of that label by relaxation

will achieve a steady state. However, the ASL signal is generally only 1% of the ΔM_b^0 signal because of the rapid relaxation of the labeled water.

By applying an amplitude-modulated off-resonance RF pulse, it is possible to acquire multiple slices with the reduction of MT effects (31). During the acquisition of the control images, a constant RF pulse is applied similar to the tagged image, but the amplitude of the RF pulse is modulated to cause the flowing spins to be inverted twice, yielding a zero net effect (Figure 1.4 c). The average power and the center frequency of the amplitude-modulated control image slice is identical to the average power and frequency of the tagged slice, therefore off resonance effects are identical to the tagged image (31,32). However, the labeling efficiency of amplitude modulated CASL is considerably less than standard CASL, typically around 68% due to imperfections in the amplitude-modulated control pulse (double inversion) (33). An alternative approach of avoiding MT effects is to use a separate RF coil placed on the neck to invert the arterial magnetization; however, this requires specialized equipment – a labeling coil and an additional RF channel that is typically not supplied with a clinical MRI system.

Pseudo-continuous ASL (pCASL) was developed to overcome the poor labeling efficiency of amplitude-modulated CASL (33,34). Continuous labeling is achieved by applying a train of closely spaced RF pulses that are applied with a pulsed gradient field. These pulses are able to achieve a flow-driven adiabatic inversion. There are a number of advantages in employing pCASL: (1) MT effects are corrected across all slices since the control and label pulses are

applied at the same location. (2) It does not require a specialized RF coil for labeling to avoid MT effects. (3) It has the ability to obtain a higher labeling efficiency (81% compared to 68% in amplitude- modulated ASL) (34).

1.3 Quantification Issues in ASL

The ASL signal is not only influenced by CBF, but can also be affected by the time it takes magnetically labeled water to reach the region of interest in the brain, as indicated by equations 1.4 and 1.5. The total transit time is generally given by two transit times. The first is the time it takes magnetically labeled arterial blood to travel from the labeling site to the arterioles in a given MRI voxel, which is labeled τ_a in Figure 1.5. The longer transit time is the time it takes labeled water to reach the capillary bed, where it can diffuse across the BBB into tissue, is labeled τ_b.

One approach for estimating the tissue transit time is by flow-encoding arterial spin tagging (FEAST). According to this technique two ASL scans are acquired: one with (ex: b = 10s/mm^2) and one without a flow-spoiling magnetic gradient. The b-value describes the strength of the diffusion gradient. The application of this gradient enables the signal from the arterial and tissue compartments to be separated. The tissue transit time (τ_b) is calculated by the following equation:

$$\tau_b = -\log\left[\frac{\Delta M''}{\Delta M}\, e^{(-wR_{1a})} - e^{(-(\Delta_{label}+w)R_{1a})} + e^{(-(\Delta_{label}+w)R_{1a})}\right] / R_{1a} \qquad (1.6)$$

Where w is the post labeling delay (described later), while $\Delta M'/(\Delta M)$ is the ratio of ASL signals with and without the diffusion gradients (35).

$$\frac{\Delta M'}{\Delta M} = \frac{\left[e^{(-\tau_b R_{1a})} - e^{(-(\Delta_{label}+w)R_{1a})}\right]}{\left[e^{(-w\,R_{1a})} - e^{(-(\Delta_{label}+w)R_{1a})}\right]} \tag{1.7}$$

A typical τ_b in humans measured by FEAST ranges from 1150 to 1550 ms from the bottom to the top slice.

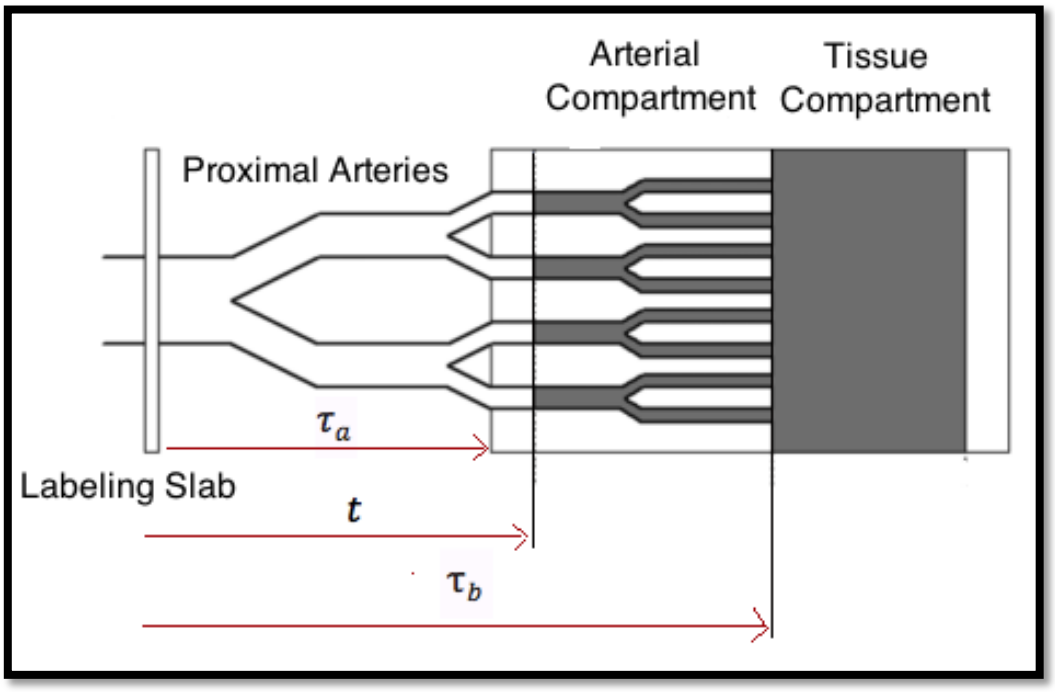

Figure 1.5: The two-compartment model for CASL consisting of the arterial and tissue compartments. The time it takes labeled blood to reach the arterial compartment is the arterial transit time (τ_a), and the time it takes for labeled blood to reach the tissue compartment is the tissue transit time (τ_b).

An alternative approach for reducing the sensitivity of the ΔM_b signal to τ_a is to add a post labeling delay (PLD) between the end of the labeling period and the beginning of the image acquisition (30). If the PLD is too short, a significant fraction of the labeled water remains in the feeding arterial compartment and the signal is sensitive to τ_a. If the PLD is optimal, then all of the labeled water will reach the tissue compartment, where exchange occurs between the capillary and the surrounding tissue. However, one must be careful in not employing an extremely long PLD which will result is a substantial loss in signal-to-noise ratio (SNR) (36).

Although the human blood volume is only 5% of the entire brain volume, the ASL signal is heavily weighted to the arterial side of the vascular system because of the rapid T_1 relaxation of the magnetic label (30). Consequently, the arterial signal in ASL can be much greater than the tissue signal, leading to 'hot spots' in the perfusion images (i.e. areas of artificially high CBF values). This effect can be accounted for by using a sufficiently long PLD to allow all of the labeled water to reach the tissue bed, or by applying diffusion gradients to suppress the vascular signal (36).

1.4 Assessing Water Exchange Across the BBB by ASL

Although ASL is a perfusion technique, it can be sensitized to water exchange across the BBB by exploiting differences in the magnetic properties of labeled water in blood and tissue (23,37,38). The fractions of labeled water in the

blood and tissue will depend on the rate of exchange across the BBB, which is characterized by the permeability surface area product (PS) of water (Figure 1.6). There are primarily two approaches to accessing water exchange between the two compartments: (1) using the difference in T_1 relaxation between blood and tissue and (2) separation of signals from the two compartments by applying diffusion gradients to suppress the faster moving magnetic spin in blood.

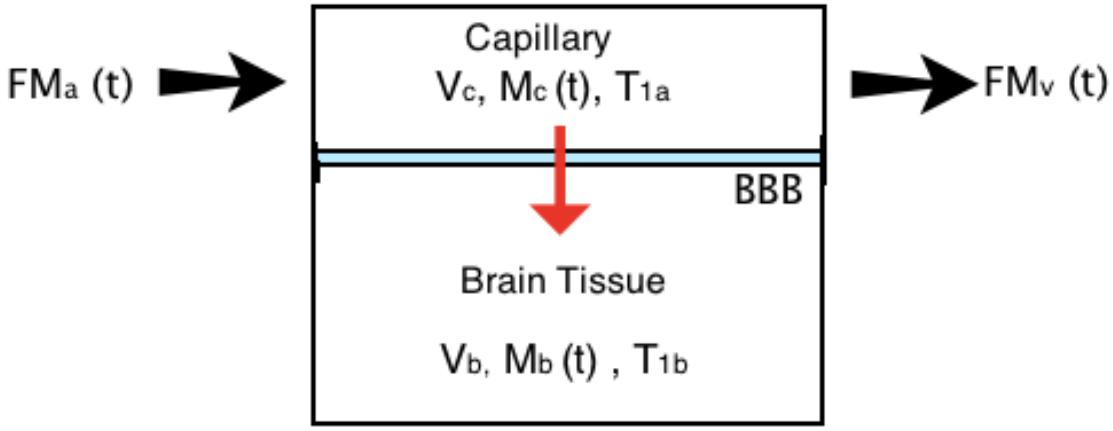

Figure 1.6: Capillary – Tissue Exchange Model. The BBB separates the two compartments. $M_c\,(t)$ and $M_b\,(t)$ represent the magnetization in the capillary and brain tissue spaces. The capillary blood volume (V_c), the longitudinal relaxation of blood (T_{1a}), the tissue blood volume (V_b) and the longitudinal relaxation of tissue (T_{1b}) are also shown for the respective compartments.

The first application in humans of the T_1 relaxation approach was by Parkes and Tofts who proposed that the rate constant characterizing water exchange could be determined by acquiring ASL data at multiple post-labeling delays, and including water exchange as an additional fitting parameter in the kinetic analysis (37). Parkes and Tofts as well as Zhou *et al*., concluded that the capillary permeability is an important factor that must be accounted for in

perfusion quantification (37,38). Further improvements to this approach include the development of techniques that account for transit time effects (39) and a two-stage method that attempts to measure the PS product of water directly (40). However, the study by Carr *et al*., questioned the precision of this approach because of the similarity in T_1 values between blood and brain tissue (41). The precision can be enhanced by using imaging methods that are also sensitive to differences in T_2 and T_2^* values between blood and tissue (42,43). Recently, Gregori *et al*. proposed a multi-echo, single-shot 3D technique to generate simultaneous images of cerebral perfusion and water-exchange (44).

The application of diffusion gradients is the second method of measuring water exchange (45–47). This approach uses weak diffusion gradients to differentiate the signal contributions from slowly diffusing water in the extravascular space and rapidly moving water in blood. Wang *et al*. adapted this approach to human applications using a relatively long PLD to allow most of the labeled spins to reach the microvasculature. The study concluded that depending on the PLD and the strength of the diffusion gradient the ASL techniques can be made sensitive to either the arterial, capillary or tissue compartments (46). Additionally, bipolar gradients with strength around 50 s/mm^2 were found to be sufficient to eliminate signal contributions from labeled water in the microvasculature. The most recent study incorporated pCASL to increase the SNR and FEAST imaging (35) to measure the arterial transit time (47). This approach will be discussed in more detail below as it forms the basis of the approach used in this thesis.

Regardless of the method used to separate the signal contributions from blood and tissue, quantification of the rate of water exchange is done by using a kinetic model that divides the total brain concentration of labeled water into two subspaces: capillary and brain tissue (Figure 1.6). The perfusion-weighted signal is then defined by the sum of labeled water in each compartment (23) :

$$\Delta M\ (t) = F.\Delta M_a\ (t) \otimes (q_c(t) + \ q_b(t)) \tag{1.8}$$

where $q_c(t)\ and\ q_b(t)$ represent the capillary and brain tissue concentrations of labeled water for an idealized impulse input of unit concentration. The symbol $\otimes$ refers to the convolution operator and originates by treating the uptake of labeled water in tissue as a linear, time-invariant system. The definition of $q_c(t)$ accounts for loss of labeled water due to the extraction of water into the tissue and T_1 relaxation.

$$q_c = \ e^{-\alpha t} \qquad\qquad t \leq \tau_c \tag{1.9}$$

$$q_c = \ 0 \qquad\qquad t > \tau_c \tag{1.10}$$

Where τ_c is the time it takes for the labeled water to travel from one end of the capillary to the other end, $\alpha = \frac{PS}{V_c} + R_{1a},\ \tau_c = \frac{v_c}{F}$, V_c is the capillary blood volume (mL/100mg) and R_{1a} is the longitudinal relaxation rate of blood. Similarly, the amount of labeled water in the tissue space is given by:

$$q_b = \beta(e^{-R_1 t} - e^{-\alpha t}) \qquad t \leq \tau_c \tag{1.11}$$

$$q_b = \beta E\, e^{-R_1 t} \qquad t > \tau_c \tag{1.12}$$

where, $\beta = \frac{1}{\left(1+\frac{\Delta R_1 V_c}{PS}\right)}$ and $E = 1 - e^{-\left(\frac{PS}{F} - \Delta R_1 \tau_b\right)}$.

$$\Delta R_1 = R_{1a} - R_{1b} \tag{1.13}$$

These equations show that the parameters α, β and *E* depend on water exchange between capillaries to tissue. The rate constant defining this exchange rate, denoted k_w, is given by (23)

$$k_w = \frac{PS_w}{V_c} \tag{1.14}$$

where, PS_w is the capillary permeability surface-area product of water (mL/100g/min) .

Because $\Delta M\ (t)$ is also dependent on the arterial input function, accurately measuring k_w requires measuring τ_a. As mentioned earlier, the two-stage approach proposed by St. Lawrence *et al*., acquired ASL images with different diffusion gradient strengths and different PLDs (47). First, arterial transit time (τ_a) is measured by the FEAST approach using a PLD delay long enough to allow all labeled water to reach the arterial compartment (800 ms) and a diffusion gradient strong enough to crush the magnetization of labeled water in the arteries (b = 10

s/mm^2). The acquisition was repeated, but with the PLD increased to 1500 ms to allow all labeled water to reach the tissue compartment and the strength of the diffusion gradient increased to 50 s/mm^2 to crush the magnetization of slow-moving labeled water in capillaries. From here onwards, this imaging technique will be referred as the diffusion-weighted ASL (DW-ASL).

When the PLD is greater than the tissue transit time, the ASL signal in the capillary space $\Delta \mathrm{M}_c\ (\mathrm{t})$ and in the tissue space $\Delta \mathrm{M}_b\ (\mathrm{t})$ are given by

$$\Delta \mathrm{M}_c\ (\mathrm{t}) = \frac{-2\mathrm{F}\ \varepsilon\ M_0}{\lambda \alpha}\ e^{-(R_{1a}-\alpha)\,\tau_b}\ \left(e^{-\alpha(t-\Delta_{label})} - e^{-\alpha t}\right) \tag{1.15}$$

$$\Delta \mathrm{M}_b\ (\mathrm{t}) = \frac{-2\mathrm{F}\ \varepsilon\ M_0\ \beta}{\lambda}\left[\frac{e^{-\ (R_{1a}-R_{1b})\tau_b}}{R_{1b}}\left(e^{-R_{1b}(t-\Delta_{label})} - e^{-R_{1b}t}\right)\right. \tag{1.16}$$

$$\left. - \frac{e^{-(R_{1a}-\alpha)\,\tau_b}}{\alpha}\ \left(e^{-\alpha(t-\Delta_{label})} - e^{-\alpha t}\right)\right]$$

where R_{1b} is the longitudinal relaxation in the brain tissue.

The assumption with DW-ASL is that $\Delta \mathrm{M}_c\ (\mathrm{t})$ and $\Delta \mathrm{M}_b\ (\mathrm{t})$ can be separated by the application of bipolar gradients because labeled water is moving faster in capillaries than static tissue. Therefore, the ASL signal collected at the two diffusion gradients (*b*) can be written simply as

$$\frac{\Delta M(\,t,b)}{\Delta M(\,t,0)} = A_1(t)\, e^{-bD_1} + A_2(t) e^{-bD_2} \tag{1.17}$$

where $A_1(t)$ and $A_2(t)$ are the fast (capillary) and slow (tissue) components of the ASL signal, and $A_1(t)$ + A_2 (t) = 1. The corresponding pseudo diffusion coefficients for the capillary and tissue labeled water are referred as D_1 and D_2.

$$A_1(t) = \frac{\Delta M_c(t)}{\Delta M_c(t) + \Delta M_b(t)} \tag{1.18}$$

$$A_2(t) = \frac{\Delta M_b(t)}{\Delta M_c(t) + \Delta M_b(t)} \tag{1.19}$$

where A_1 and A_2 are written as functions of time because their values will change depending on the PLD. As the labeled water diffuses from the capillaries in to the tissue, A_1 decreases in the presence of a long PLD. Assuming the capillary contribution is suppressed when the diffusion gradient is applied (b_{DW}), then A_1 and A_2 can be written as,

$$A_1(t) = 1 - \frac{\Delta M\,(b_{DW})}{\Delta M(b_0)} \tag{1.20}$$

$$A_2(t) = \frac{\Delta M\,(b_{DW})}{\Delta M(b_0)} \tag{1.21}$$

The fraction of labeled water in the tissue and capillary spaces, as defined by A_1 and A_2, will depend on k_w and τ_b. The latter is determined separately by the FEAST data.

Applying this technique on healthy human subjects (47), a PLD of 1500 ms was chosen to allow all labeled water to reach the capillary space as confirmed by average τ_a of 1.49 s for whole-brain grey matter. The average k_w value was 110 min^{-1} for grey matter and 126 min^{-1} for white matter. Using an assumed value for the capillary blood volume (V_c), PS_w ranged between 165 to 220 mL/100g/min, in reasonable agreement with values measured by positron emission tomography.

The main challenge to measuring k_w is achieving an acceptable degree of precision due to the inherently poor SNR of ASL. The rapid T_1 relaxation of labeled blood is the primary reason for the poor sensitivity. To overcome this issue, investigators have used relatively long acquisition periods (~10 min), employed a echo-planar imaging (EPI) or spiral imaging techniques to reduce motion artifacts, used higher field strengths to enhance relaxation time differences between blood and tissue, and used phased array RF coils to improve sensitivity.

1.5 Opening the Blood-Brain Barrier

An established approach for opening the BBB is to inject mannitol intracarotidly. The rapid elevation in plasma osmolality causes the endothelial cells to shrink, leading to openings in the TJs (Figure 1.7). Increased BBB permeability following carotid infusion of mannitol (25%) has been shown in a number of animal species including rats and rabbits (48,49). However, the results have not been consistent, with variations in magnitude and distribution of BBB disruption reported (50).

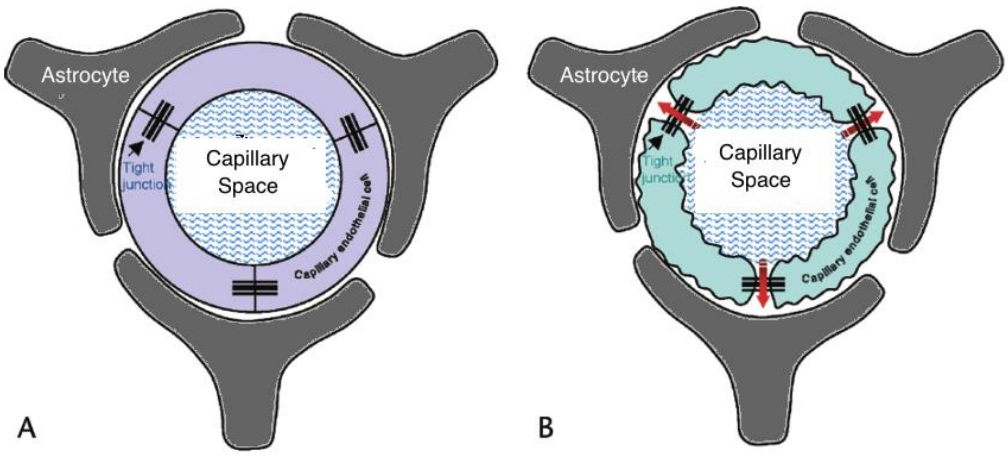

Figure 1.7: (A) Before and (B) administrating an osmotic agent. Injection of The hyperosmolar osmotic reagents leads to shrinking of the endothelial cells and subsequently enlarges the pore size by opening the TJs. Adapted from Rebeles, F *et al*., 2006 (52)

In swine, the effects of mannitol are even less conclusive. Anwar *et al.,* reported no increase in regional BBB permeability in newborn pigs. Marchi *et al.,* were able to open the BBB in adult pigs, as demonstrated by contrast-enhanced

MRI and Evans Blue staining. However, only one third of the experiments showed noticeable disruptions and these were characterized by a patchy distribution of leakage spots (51). Considering that piglets were selected for these experiments (see Section 1.8), a more consistent method of opening the BBB at specific locations in the brain is required.

1.6 Introduction to Focused Ultrasound

Focused ultrasound (FUS) was initially proposed in the 1940's as a method of producing focal heating with minimal effect on surrounding tissue (53). It is now used to deliver thermal therapy to a number of cancers including brain (54), breast (55,56), bone (57,58), and prostrate (59–61). Bakey *et al*., first proposed the concept of using high-intensity FUS to open the BBB in 1956, and there were a few studies reported over the next few decades. However, the feasibility of the approach improved dramatically with the advent of low-frequency pulsed FUS applied in the presence of encapsulated gas-filled microbubbles (MBs) (diameter ≤ 8 μm) (62). Blood-brain barrier disruptions (BBBDs) are caused by the interactions between sonicated MBs and the layer of endothelium lining the BBB. At lower pressures, tissue damage and skull heating is avoided and BBBDs are transient, typically closing within 24-hours (63). The two primary mechanisms that contribute to BBBD are radiation pressure and cavitation.

1.6.1 Mechanisms for Blood-Brain Barrier Disruption: Acoustic Cavitation and Radiation Pressure

Acoustic cavitation refers to the phenomenon of formation and collapse of gaseous cavities due to the interaction with an ultrasound wave. That is, MBs in the blood stream will contract and expand with the compression and rarefaction points in the ultrasound wave. The severity of the interaction depends on the frequency, pressure amplitude and duration of the sonication, as well as the size and volume of the gas bubbles (64).

Shear stress or radiation force (Figure 1.8) plays a significant role in advocating stable cavitation to disrupt the BBB when the acoustical pressure limits are low (65). Inertial cavitation will occur if the ultrasound intensity (or high acoustical pressure) exceeds a threshold pressure. This threshold is typically around 0.45 MPa when ultrasound is delivered transcranially (65,66). Rapid growth and collapsing of MBs can induce temperature elevations, high velocity jets and shear stress, all leading to tissue damage (62,64). Therefore it is best to avoid reaching high acoustical pressures as they lead to permanent BBBD.

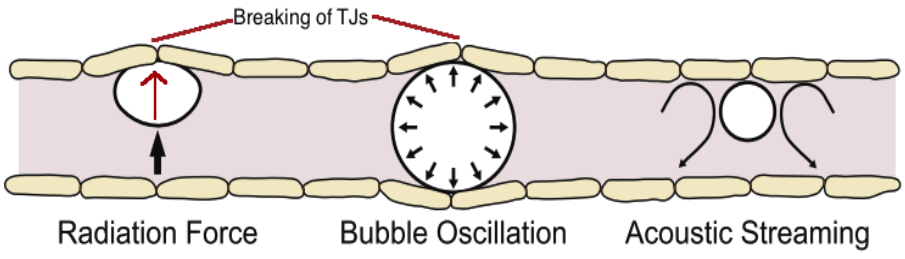

Figure 1.8: Possible mechanisms for BBBD via FUS and MBs: TJ separation by radiation force, bubble oscillation or by acoustic streaming. Adapted from Vykhodtseva, N *et al*., 2008 (62)

1.6.2 The Role of Microbubbles in Focused Ultrasound

The injection of MBs prior to sonication for the purpose of generating bubbles in the brain blood vessels to aid BBBD was first suggested in 2001 (63). Hynynen *et al.*, injected an IV bolus of Optison (GE Healthcare, Milwaukee, WI) and demonstrated that the BBBD they witnessed had no neuronal damage, was reversible, and the acoustic pressure was two orders of magnitude lower than what was typically needed for tissue ablation (63,67). The BBBD is correlated to the interaction between the ultrasound field and the MBs. MBs have been able to reduce the acoustic energy requirement and avoid overheating of the skull during FUS BBBD (68).

There are 3 brands of commercially available MBs in the world market namely Definity (Lantheus Medical Imaging, MA, USA), Sonovue (Bracco Diagnostics Inc, Milan, Italy) and Optison (GE Healthcare, WI, USA). However, only Definity MBs are available for use in North America, they have been used in this study. All 3 types of MBs are micron-sized and filled with a perfluorocarbon gas, surrounded by either an albumin or a phospholipid layer. Definity MBs are filled with Octafluoropropane (OFP, C_3F_8) covered by a phospholipid shell and are between the diameters of 1.1-3.3μm with a half-life of 1.3min (68,69). The diameter of the MBs is a critical factor in the amount of BBBD achieved as well as in the reversibility of the disruption.

Additional factors such as resonance frequency, pressure threshold for cavitation, bubble expansion ratio, lifetime of stable cavitation and duration of

opening are all determined by the diameter of the MB (65). Larger bubbles exert a stronger shear stress on the capillary wall in comparison to smaller bubbles. On the other hand, the acoustical pressure demand by a small bubble would be much larger to reach the same bubble expansion achieved by a larger bubble (70). Additionally, previous studies have also found that the pressure threshold for BBBD with inertial cavitation falls between 0.30 - 0.45 MPa for MBs in the 1-2-μm range while BBBD with stable cavitation using MB sized between 4-5 and 6-8 μm holds a pressure threshold of 0.15 - 0.30 MPa (66). However, the expansion of a MB is inversely proportional to its diameter; therefore, it is beneficial to use smaller MBs (1-2μm) if one requires the BBB to recover faster. It is also known that MBs smaller than 2.5 μm are not capable of opening the BBB in sites away from the larger vessels due to bubble fragmentation, even before the MBs have reached the microvasculature which feeds the endothelium (65).

In terms of MB dose the FUS community is divided; one study revealed that MB dose had no effect on the volume of BBBD (71), while several studies have stated that the volume of BBBD increased as they increased the MB dose (72–74). In summary, the resonance frequency, shear stress, permeability, and BBB recovery time decrease with decreasing MB size, while the pressure threshold and the expansion ratio increases.

1.6.3 The Effect of Acoustic Parameters of Ultrasound

The effect of various acoustic parameters on the volume of observed BBBD have been extensively studied. The volume of BBBD and BBB recovery time both increased with increasing pressure of the incoming ultrasound wave. However, one study that used a 1.08 MHz transducer with sonication times of ~300 s witnessed that BBBD was reduced at pressures > 0.5 MPa. They concluded that successful delivery of agents across the BBB increases only when the pressure is less than the threshold for generating a lesion (~0.45 MPa) (75). The same team also experimented on the effect of sonication time on the amount of BBBD created and noticed that the BBBD effects plateaued after reaching a sonication time of 600 s (75). One must also note that increased sonication times result in increased degree of damage to the tissues.

As the frequency of the ultrasound transducer is increased the pressure threshold to generate BBBD increases. When the frequency of the transducer matches the resonance frequency of the MBs, the transfer of energy from the ultrasound wave to the MB occurs effectively to cause a BBBD (65).

The relationship between the pressure threshold and frequency for effective BBBD without causing lesions is approximately equal to a Mechanical Index) MI of 0.46 (71)

$$Mechanical\ Index\ (MI) = \frac{Peak\ Negative\ Pressure}{\sqrt{Frequency}} \qquad (1.22)$$

The relationship between the pulse length and the BBBD has also been widely studied. The BBBD is reduced when the pulse lengths are shortened (<1 ms), however increment of closely timed short pulses enhances the BBBD (61,66). Longer pulses created more BBBD (63,77) and it has been suggested this could be possibly due to radiation pressure caused on the endothelium (22).

1.6.4 Challenges to Disrupting the Blood-Brain Barrier by Focused Ultrasound

The skull is the major obstacle in delivering ultrasound waves to the brain. Because the skull bone is heterogeneous and is unevenly shaped, almost 90% of the propagating FUS wave is lost (64). The speed of sound in the skull is ~2900m/s, twice that of water and because the thickness is varied the speed of sound differs at different locations (78). The relatively high speed of sound coupled with variable thicknesses distorts wave propagation and destroys the focus of the ultrasound beam. Additionally, beam refraction can occur if the ultrasound beam causes a non-normal incidence to the skull. Due to the above challenges early research in the field was performed with a craniotomy to deliver ultrasound to the brain.

Furthermore, because the acoustic impedance of bone is much different from water or soft tissue there are energy losses at the bone-tissue interface. At low frequencies reflection is the cause for majority of energy losses. However, at high frequencies scattering and absorption dominate. FUS delivery through the

skull over the frequency of 1 MHz is next to impossible unless performed through an acoustic window or by transcranial Doppler ultrasound. Acoustic windows are an area of the brain where the skull bone has not yet developed. Therefore, in newborns ultrasound scans can be performed through the anterior fontanelle and in adults through the temporal or the suboccipital windows (78).

Lastly, the reflective nature of the skull bone can create standing waves during long sonication times. Standing waves create unanticipated hot spots especially in healthy tissue and are a major concern in therapeutic FUS due to the causation of hemorrhage. The amount of observed standing waves increased as the frequency of the transducer decreased (79). Although small aperture arrays create significant amounts of standing waves, large aperture arrays (up to 1372 elements) in a tightly focused transducer (lower f-number) with a reduced duty cycle in pulsed mode will reduce skull heating, allow beam focusing and lessen standing waves (80).

Recent studies have shown that the life of the MBs while circulating in the microvessels decreased 3-times faster when Isoflurane is used with oxygen as the carrier gas instead of medical air (81). Another study states that Definity MBs act as an osmotic agent swelling up bringing in oxygen and nitrogen in to the MBs. This is because Definity MBs are filled with OFP, which has low plasma solubility. However, when MBs are in close proximity of the pulmonary system, OFP in the MBs equilibrate with the gas in the alveolar space, OFP is lost and exhaled even before sonication has been completed (82). Moreover, as the OFP gas content in the MB decreases through time, the surface tension and the

ultrasound peak pressure increases. As the FUS wave propagates through the MB, the vapor pressure of OFP goes over the threshold converting OFP gas to liquid (81).

Although the loss of OFP in the alveolar space diminished the MB survival, the addition of the OFP can prolong the MB survival. Using medical air as a carrier gas in conjunction with Isoflurane during the sonication process can improve the MB survival.

1.7 Porcine Studies to Date

So far there have been three groups that have investigated ultrasound induced BBBD in a swine brain. However, out of these studies only one has been conducted by using focused ultrasound while two studies have been under unfocused ultrasound, thus our study would contribute to determining FUS parameters for a swine model.

One study involved 24 adult pigs anesthetized under Isoflurane whom were sonicated transcranially through the temporal bone with a 1 MHz unfocused transducer, with a pulse duration of 2 ms and a pulse repetition frequency (PRF) of 100 Hz. The intensity of the transducer was 2 W/cm^2 and the duty cycle was maintained at 20%. The MBs used in this study were lipid encapsulated (ImaRx Therapeutics, AZ, USA) and perfluorocarbon-exposed sonicated dextrose albumin (PESDA) that were prepared on site. The BBBD was short lived, up until 30 min and after 120 min they were not able to detect a significant uptake of

evans blue (EB). There was also no significant uptake of Gd-DTPA after 120 min. The decrease in peak negative pressure by 10-times was blamed on beam attenuation due to sonication through an intact pig skill. Additionally, the BBBD achieved in this study was short-lived, while an insignificant uptake of EB was also observed (83).

A group in Taiwan sonicated 10 adult pigs with a 28 kHz (low-frequency) commercially available system (K-Sonic Inc., Taiwan) that were anesthetized under chlorohydrate (30 mg/kg). The sonication parameters include a burst length of 30 ms (group1, n=3) or 100 ms (group 2, n=3), PRF of 1 Hz and a sonication time of 5 min. A craniotomy was conducted to position the 28 kHz ultrasound probe and MBs used were Sonovue (0.05 mL/kg). Prussian blue stained sections confirmed that the 30 ms bursts successfully disrupted the BBB in two out of three of the animals while the disrupted regions itself were larger in all three of the animals treated with 100 ms bursts. However, the T_2^* images of the group 2 animals indicated hemorrhage and H&E staining also confirmed by showing large scale erythrocyte extravasation (84).

The only study on pigs to date using a focused ultrasound transducer sonicating at a frequency of 0.4 MHz (Imasonics, France) with the assistance of a neuronavigation system (Stryker, Germany) found that a negative pressure of 0.43 MPa resulted in consistent BBBD. The FUS parameters were a burst length of 10 ms, a PRF of 1 Hz for a sonication time of 30 s. However, this study was also conducted after a craniotomy and the use of a 3x3 grid pattern to perform the sonication points fed in to a successful BBB opening (85).

1.8 Objectives, Rationale and Overview of the Project

The overall goal of the project was to determine if a novel ASL technique is sensitive to changes in the BBB. Since pCASL images suffer from poor spatial resolution (3.75 x 3.75 x 8 mm^3), it is important for this study to choose an animal model with a reasonably large brain such that it could be imaged in a 3.0 T MRI scanner, which is the same field strength used in previous human studies (46,47). Therefore, piglets were chosen for this study. To test the sensitivity of the technique, a reliable method of opening the BBB at known locations was required. For this purpose FUS was selected over osmotic agents such as mannitol.

Although FUS-assisted BBBD has been explored, the effectiveness of the disruption depends on multiple factors including the animal model, ultrasound power, sonication time, MB concentration, incidence angle of the ultrasound wave and gas exchange effects due to the selected anesthesia protocol. Therefore, as a secondary objective of this study, preliminary experiments were conducted to select the optimal FUS parameters to open the BBB in a piglet.

Chapter 2

2 Materials and Methods

2.1 Animal Preparation

This research study was approved by the Animal Use Subcommittee of the Canadian Council of Animal Care at Western University. Experiments were performed on Duroc piglets (1-5 days old, mean weight of 2.13 ± 0.28 kg) obtained from a local supplier on the morning of the experiments. Each piglet was anesthetized with Isoflurane (4-5%) during preparatory surgery and stabilized after with 2-3% Isoflurane. The animal was tracheotomized and mechanically ventilated on an oxygen and medical air mixture. A 22 gauge catheter, was placed in a ear vein to infuse Gd-DTPA, MBs, and EB. Once the animal was ventilated, a femoral artery line was surgically placed to monitor mean arterial pressure (MAP) and to extract blood samples to measure arterial CO_2 and O_2 tensions ($PaCO_2$ and PO_2, respectively) as well as the glucose concentration. Heart rate (HR), pH, and rectal temperature were also monitored. The temperature was maintained between 37.5°C and 38.5°C by a recirculating water heating pad.

Following the surgical procedure, the piglet's head was shaved and placed on a custom-built platform with an opening to expose the head to the focused ultrasound wave. To avoid the formation of standing waves and reduce energy loss due to refraction, the head was oriented such that the incidence angle of the

FUS wave was normal to the skull. The head was secured to avoid any head movements during the experiment.

2.2 Experimental Procedure

2.2.1 Sonication Protocol

Sonication was performed using an MRI-compatible, image-guided focused ultrasound system with a three-axis positioning system, which is capable of delivering focused ultrasound to precise locations in soft tissue (FUS instruments Inc., Toronto, ON) (Figure 2.1). The transducer is spherically focused and has a diameter of 7 cm (f-number = 0.8). It is able to target with a 0.1 mm precision and can sonicate up to a maximum power of 9 W (1.88 MPa).

Figure 2.21: Left: The monitor that displays the GUI. Middle: The FUS system that is filled with degassed water. Right: The electronics cart consisting of the controls and power supply. (*Images from http://www.fusinstruments.com*)

The FUS system was placed on the bed of a 3T Biograph mMR scanner (Siemens Healthcare, Erlangen, Germany). The tank housing the transducer was filled with degassed water. The FUS system was co-registered to the MRI with the assistance of a calibration plate supplied with the FUS system. The left / right, anterior / posterior and head / foot positioning of the focal spot in the calibration plate was entered on the FUS system as the center of the transducer.

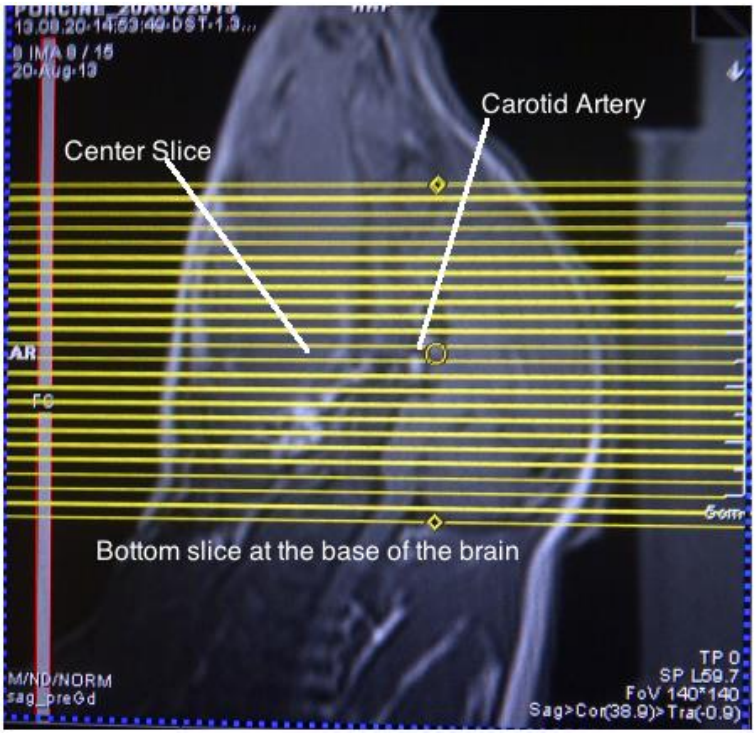

Figure 2.22: Locations of the axial T_1-weighted images, which were defined using landmarks identified in the sagittal images.

After the application of ultrasound gel to the piglet's head, the piglet was placed supine on an experiment plate with an acoustic window. The position of the brain was defined by acquiring a coronal localizer image using a 4-channel flex coil wrapped over the piglet's head. Next, a set of sagittal T_1-weighted

images (TR/TE: 500/12 ms, matrix size: 128 X 128, FOV: 140 mm, 15 slices of thickness 2.5 mm and spacing of 0.25 mm) were acquired to select the axial slice position for sonication. A set of axial T_1-weighted images was acquired (TR/TE: 500/12 ms, matrix size: 128 X 128, FOV: 128 mm, 23 slices of thickness 2.5 mm and spacing of 0.25 mm). The position of these images were chosen based on landmarks in the sagittal images and arranged such that the location of the most distal image touched the base of the brain and the center slice coincided with a bright blood vessel (Figure 2.2). Sonication was performed in two consecutive slices near the centre where the brain was the largest.

The transducer was operated at a frequency of 0.563 MHz and at a pulse rate of 1 Hz with 10 ms burst length for 1% duty cycle for each sonication. Six sonications were performed in a grid pattern in the right hemisphere at 2 mm spacings. The pattern was repeated on a consecutive slice 2.5 mm apart, for a total of 12 sonications (Figure 2.3).

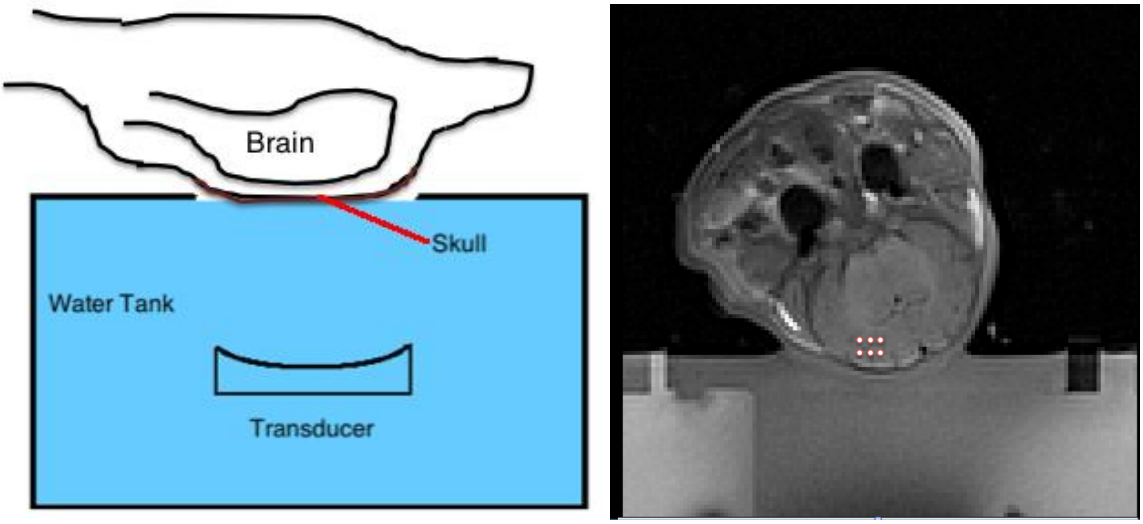

Figure 2.3: Schematic diagram of the FUS set up during sonication. Right: T_1-weighted MR image showing the location of six targeted points.

A single bolus of Definity MBs (Lantheus Medical Imaging, MA, USA) at a dose of 0.02 mL/kg was intravenously injected through the ear vein at the start of each sonication. Each sonication was 120 s, and partial pressure of oxygen (PaO_2) was maintained between 70-90 mmHg to prolong the MB survival in the vasculature. The total sonication time, including a minute delay between successive sonications, was 36 minutes. PaO_2 was increased to greater than 100 mmHg once the sonication was completed.

2.2.2 Permeability Imaging Protocol

After sonication, the piglet was lifted off the FUS system, while remaining strapped to the platform, and the FUS system was removed from the scanner. The piglet was placed in a 15-channel, 154-mm diameter transmit/receive coil supplied by the manufacturer. The platform was carefully leveled to replicate the position of the head during sonication. A set of sagittal T_1-weighted images with the same imaging parameters as before was acquired to landmark the location of the sonicated region. The location was confirmed by acquiring a set of axial T_1-weighted images (named the pre Gd-DTPA images) using the same imaging parameters used with the flex coil.

A schematic diagram of the DW-ASL sequence used in this study is shown in Figure 2.4. The sequence is a combination of pCASL and twice-refocused spin-echo diffusion echo-planar imaging. The pCASL sequence consisted of a train of 1600 Hanning-shaped RF pulses with a pulse duration of

500 μs, a spacing of 920 μs, peak B_1 of 5.3 μT, and an average B_1 of 1.8 μT. The RF pulses were implemented in conjunction with a slice selective gradient of 6.0 mT/m for a total labeling time of 1.5 s. The labeling plane was placed 4 cm below the center of the imaging volume. This distance was selected because the carotid arteries are straight at this location, as confirmed by MR angiograms acquired in preliminary experiments. The DW-ASL sequence includes a PLD in which two nonselective inversion pulses are applied to suppress the static magnetization. Diffusion gradients with b-values of 0 and 50 s/mm^2 were applied along the slice direction.

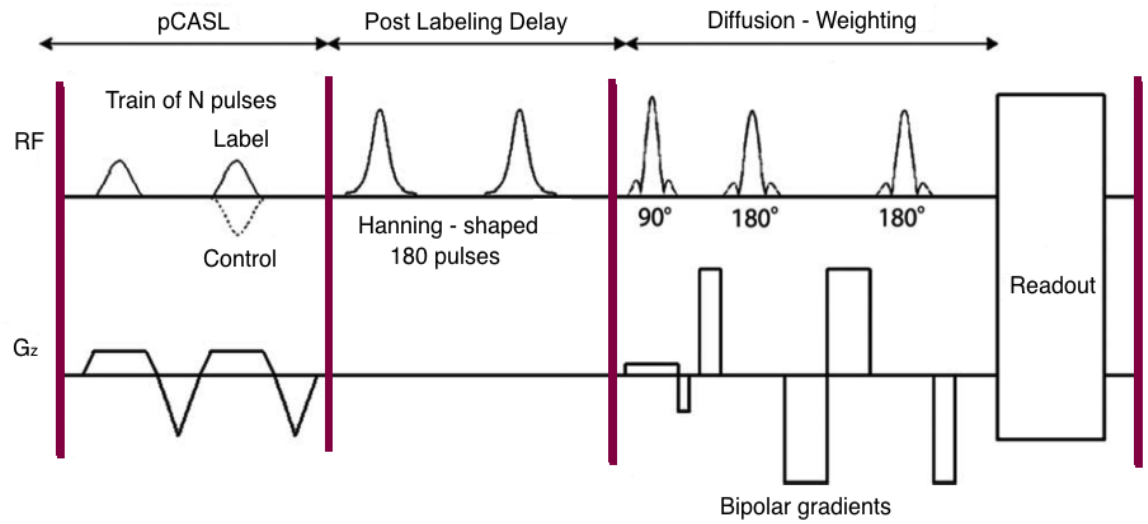

Figure 2.4: The DW-ASL sequence is a modification of the standard pCASL technique. DW-ASL consists of pCASL with a twice-refocused spin-echo diffusion imaging sequence. Adapted from St. Lawrence *et al*., (47)

The ASL images were positioned such that the middle slice was centred on the sonicated region as determined from the axial T_1-weighted images. Both the FEAST and DW-ASL images were acquired with the following imaging parameters: FOV = 240 mm, matrix = 64 x 64, BW = 2790 Hz/pixel, 7/8 partial k-space, GRAPPA = 2, slice thickness = 8 mm, inter-slice gap = 1.28 mm, 7 slices, TE = 48 ms, and TR = 3500 ms. FEAST data were acquired with b values of 0 and 10 s/mm^2, PLD = 500 ms, and 96 acquisitions. DW-ASL images were acquired with b values of 0 and 50 s/mm^2 (96 and 192 acquisitions, respectively) and a PLD = 1000 ms.

Following the ASL imaging, T_2^*-weighted images were acquired to detect any hemorrhaging caused by the sonication (TR = 90 ms, Flip Angle = 20°, first TE = 4.92 s, echo separation = 5.17 s, number of echoes = 10, BW = 260 Hz/pixel, matrix size = 128 X 128, and FOV = 128 mm). One 5 mm thick slice was acquired centered on the sonicated region. Finally, Gd-DTPA was injected intravenously (0.2 mL/kg; Magnevist, Bayer Healthcare Pharmaceuticals, NJ, USA) and axial T_1-weighted images (i.e. post Gd-DTPA images) were acquired with the same parameters as before.

Each piglet was administered 1.5 mL/kg of EB (Sigma-Aldrich, MO, USA) approximately 2.5 hours after sonication. The piglet was euthanized 1 hour after the injection, and the brain harvested and fixed in formalin for at least 48 hours.

2.2.3 Optimization of the FUS Power

Experiments were conducted at three FUS power groups categorized as low power (1.5 W), medium power (2.5-3 W) and high power (6.0 W) (0.7, 0.97, 1.53 MPa, respectively) to determine the power setting sufficient to open the BBB without causing hemorrhage. Increased BBB permeability was assessed by acquiring T_1-weighted images following Gd-DTPA injection and by histological staining with EB dye. Evidence of hemorrhage was assessed by EB staining and by T_2^*-weighted imaging. All experimental and imaging details were the same as outlined in section 2.2.2.

2.3 Data Analysis

The change in signal intensity caused by the leakage of Gd-DTPA was determined by drawing a region of interest (ROI) around the 12 sonication locations on the post Gd-DTPA T_1 images. For comparison, the ROI was superimposed on the contralateral side of the image to determine the signal intensity in a non-sonicated region. Individual intensities in each ROI were extracted using an in-house Matlab code (Mathworks, MA, USA). The ROIs of the sonicated regions were guided by the original left/right, anterior/posterior and head/ foot positioning of the 12 target locations that were obtained off the MRI scanner for each piglet. A ratio between the sonicated ROI intensity to non-sonicated ROI intensity was taken for each piglet.

The T_2^* value at a given power was calculated by fitting a single exponential function to the multi-echo data:

$$\ln\left[\frac{S}{S_0}\right] = -R_2^*.(TE) \tag{2.1}$$

where S is the signal in the sonicated region at a given echo time, S_0 is the signal at TE = 0, and $R_2^* = \frac{1}{T_2^*}$.

Raw EPI FEAST and DW-ASL images were co-registered to the T_1-weighted images using SPM software (Statistical Parametric Mapping, London, UK). In Matlab, the registered EPI images were pair-wise subtracted and time averaged to generate mean ASL (ΔM) images for each b value in the FEAST and DW-ASL data sets. ROI analysis was used to determine the ratios $\Delta M_{b_{10}}/\Delta M_{b_0}$ and $\Delta M_{b_{50}}/\Delta M_{b_0}$ from the FEAST and DW-ASL, respectively, for whole brain and for the sonicated and the non-sonicated regions defined in the T_1-weighted images. These ratios were used to calculate estimates of the arterial transit time (τ_b) and the water exchange rate constant (k_w) in each ROI. τ_b was calculated from Eq. 1.6 using an assumed blood T_1 of 1.49 s (47) and accounting for a time delay of 0.065 s between the acquisitions of successive slices. k_w was determined by comparing the measured capillary fraction, A_1, to a table of values generated from Eq. 1.18 and Eq. 1.19 over a range of k_w values (0.01 to 500 min^{-1}) using the calculated τ_b value and assumed T_1 values of blood (1.49 s) and brain tissue (1.26 s).

2.4 Statistics and Sensitivity Analysis

Paired sample t-tests were used to compare measurements from the sonicated and non-sonicated ROIs. Comparisons were conducted for signal intensities in the contrast-enhanced T_1 images, the $\Delta M_{b_{50}}/\Delta M_{b_0}$ ratio and k_w values from the DW-ASL data. Differences with $p < 0.05$ were considered significant.

The signal-to-noise ratios (SNRs) of the FEAST and DW-ASL sequences were characterized by measuring the temporal standard deviation in the ΔM series. The SNR in each pixel was first calculated as the ratio of the mean signal, M_p, to the corresponding standard deviation, σ_{Mp}. The final image SNR was defined as the average value across all pixels in the whole brain ROI.

Chapter 3

3 Results

3.1 Optimization of the FUS Power

Data were acquired from a total of 11 animals: 2 in the low-power group (1.5 W), 6 piglets in the medium-power group (5 at 2.5 W and 1 at 3 W) and 3 in the high-power group (6 W). All animals were maintained at normal $PaCO_2$ between 37 to 42 mmHg (40.63 ± 3.54 mmHg), and normal PaO_2: 70 to 90 mmHg during sonication (79.42 ± 7.90 mmHg) and above 100 mmHg during ASL. Mean heart rate was 144.33 ± 24.30 and blood glucose was always kept above 4 mmol/l.

Figure 3.1 shows selected slices of post Gd-DTPA T_1-weighted images and T_2^*-weighted images. Evidence of disruptions to the BBB is visible in the post Gd-DTPA images, as seen from the enhanced intensity in the target area of sonication (marked by the yellow arrows). Blood-brain barrier permeability increased with sonication power as shown in Figure 3.2. This graph presents the average signal ratio at the three powers for the sonicated ROI to the non-sonicated ROI from the post Gd-DTPA T_1-weighted images. A significant increase in signal intensity in the sonicated ROI compared to the non-sonicated ROI was found at the medium and high power levels.

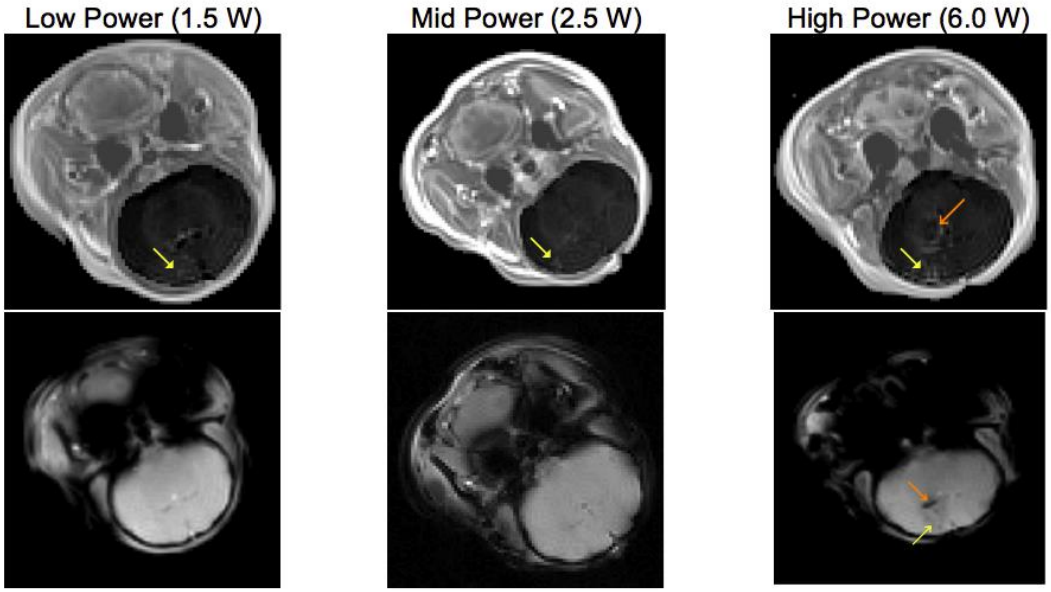

Figure 3.1: T_1 and T_2^*-weighted images at the three sonication powers. Row 1: Post Gd-DTPA T_1 images, Row 2: T_2^*-weighted images. The yellow arrows indicate the BBB opening while the orange arrows indicate the hemorrhage at the ventricles

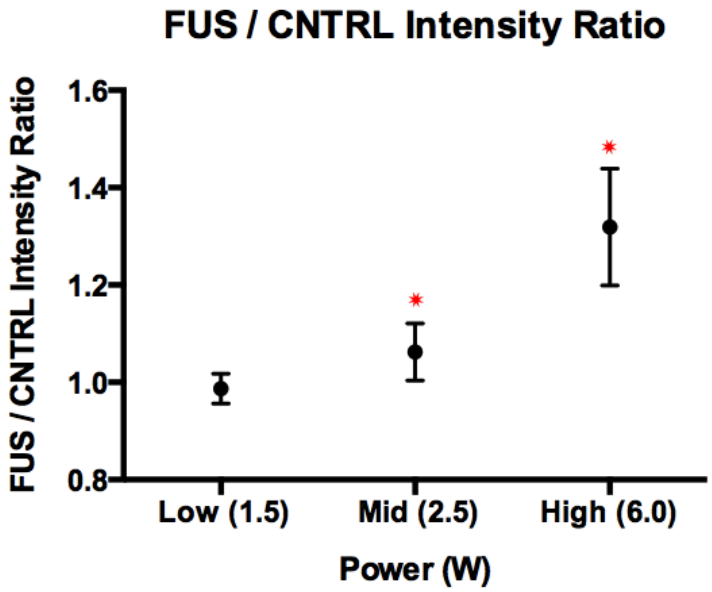

Figure 3.2: Ratio of the signal intensity from the post Gd-DTPA T_1-weighted images from the sonicated ROI to the non-sonicated ROI plotted against the FUS power. Asterisks indicate significant signal increase between the two ROIs.

The post Gd-DTPA image enhancement caused by BBBD was evident by EB staining as shown in Figure 3.3. Although qualitative, there was minimal evidence of leakage at the lowest power; whereas, EB staining was observable at the medium and high power groups.

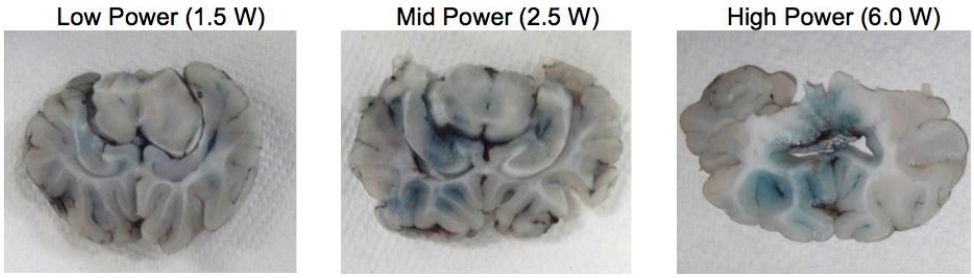

Figure 3.3: Histology with Evans Blue dye seen on tissue sections that corresponded to the targeted FUS slices.

Although Figure 3.2 illustrates that the greatest increase in BBB permeability was observed at an FUS power of 6 W, the problem with using too high of a power setting is the possibility of causing hemorrhaging, which could affect the signal intensity in the ASL images through a change in the tissue T_2^*. Evidence of hemorrohaging was observed in the T_2^*-weighted images displayed in the second row of Figure 3.1. While only one set of T_2^*-weighted images were collected at 6 W, hemorrhaging resulted in a lower signal intensity observed in the sonicated ROI and a signal void around the ventricle near the ROI (dark region in Figure 3.1 highlighted by the orange arrow). In contrast, T_2^*-weighted images collected for all animals in the low and medium power groups were uniform and showed no evidence of ventricular bleeding.

Potential signal changes caused by bleeding were investigated by measuring T_2^* in the sonicated and non-sonicated ROIs. Figure 3.4 displays the signal intensity from the T_2^*-weighted images in the sonicated ROI at 6 W and in both ROIs at the medium power. The similarity in signal decay between the sonicated and non-sonicated ROIs for the medium power group suggests this power level wasn't sufficient to cause hemorrhaging. This was confirmed by the average T_2^* values given in table 3.1, which showed no significant difference between sonicated and non-sonicated ROIs at the low and medium power. In contrast, the noticeably faster decay in the sonicated ROI at 6.0 W likely reflects a decrease in tissue T_2^* due to the leakage of red blood cells. For this animal, a lower T_2^* value was measured in the sonicated ROI compared to non-sonicated side (Table 3.1).

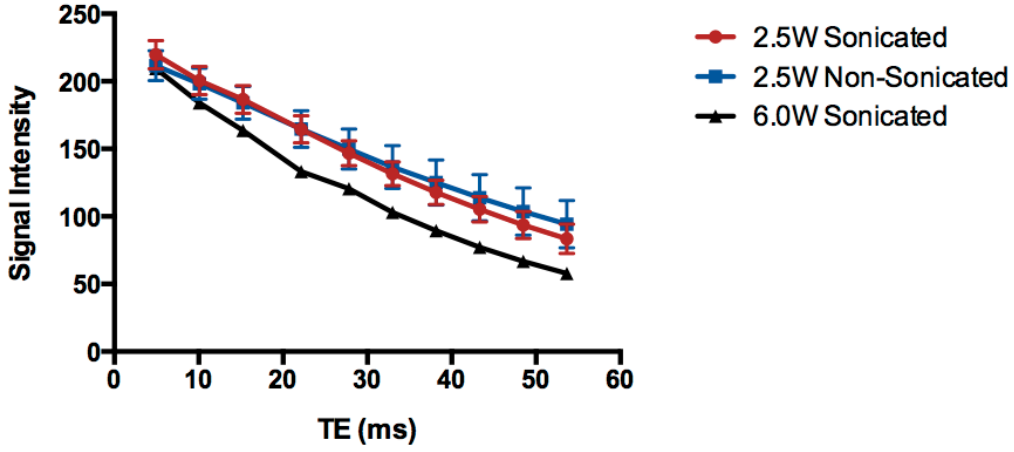

Figure 3.4: Signal decay curves from the T_2^*-weighted images at 2.5 W (sonicated and non-sonicated ROIs) and 6 W (sonicated ROI). The 2.5-W data were averaged over 6 animals; whereas, the 6.0-W data were acquired from one animal.

Table 3.1: T_2^* values of the sonicated and non-sonicated regions for all power groups

	T_2^* Sonicated Region (ms)	T_2^* Non-Sonicated Region (ms)
Low-Power	46.10 ± 5.52	55.94 ± 13.33
Medium-Power	59.52 ± 10.01	50.00 ± 7.67
High-Power	39.84	51.28

3.2 DW-ASL Results

A total of 5 piglets from the medium-power group were used in the FEAST analysis, as FEAST data were not collected on one piglet. However, data from all 6 animals were used in the DW-ASL analysis. Figure 3.5 illustrates one set of a post Gd-DTPA T1-weighted image and the corresponding coregistered b = 50 s/mm^2 DW-ASL image.

Average $\Delta M_{b_{10}}/\Delta M_{b_0}$ and $\Delta M_{b_{50}}/\Delta M_{b_0}$ ratios across the whole brain were 0.53 ± 0.13 and 0.53 ± 0.08, respectively. Individual whole-brain τ_b and k_w values from every piglet are presented in Table 3.2. The average τ_b for the whole brain was 1.06 ± 0.12 s and the average whole-brain k_w was 106 ± 15 min^{-1}.

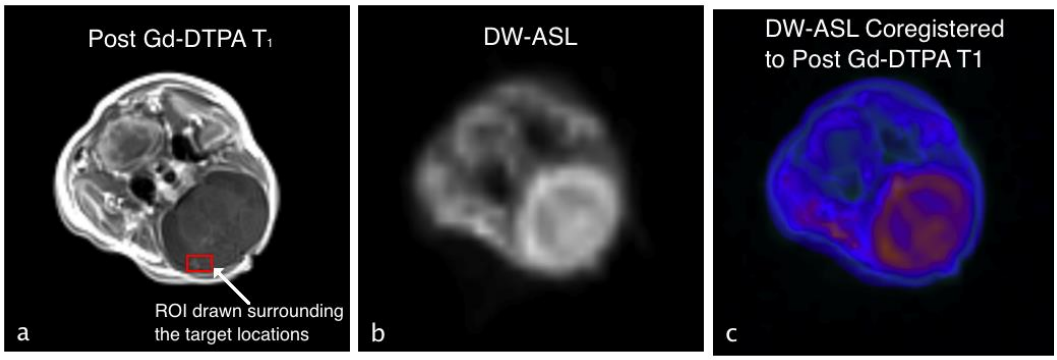

Figure 3.5: a) Sonicated ROI as shown on the post Gd-DTPA $\boldsymbol{T_1}$-weighted image. b) Corresponding co-registered b = 50 s/mm^2 DW-ASL image. c) The fusion of the DW-ASL and the $\boldsymbol{T_1}$-weighted images to demonstrate the overlap. The coregistration image is produced using MRIcron (Neuroimaging Tools and Resources, McCausland Center for Brain Imaging, SC, USA).

Table 3.3: Whole-brain average tissue transit time ($\boldsymbol{\tau_b}$) and water exchange rate ($\boldsymbol{k_w}$)

Piglet	τ_b (s)	k_w(min^{-1})
1	1.09	97
2	0.93	118
3	0.95	100
4	1.11	129
5	1.23	106
6	-	86
Mean	1.06 ± 0.12	106 ± 15.43

FEAST and DW-ASL images from one piglet are shown in Figure 3.6. These images have been masked to isolate the brain and were smoothed with a 7-mm Gaussian kernel for visualization. Each set of images includes the ΔM_{b_0} image in the first row, the $\Delta M_{b_{DW}}$ image in the second row, and the ratio image of $\Delta M_{b_{DW}}/\Delta M_{b_0}$ in the third row. For this example, whole-brain $\Delta M_{b_{10}}/\Delta M_{b_0}$ and $\Delta M_{b_{50}}/\Delta M_{b_0}$ were 0.66 and 0.64, respectively.

Individual $\Delta M_{b_{50}}/\Delta M_{b_0}$ values and the corresponding k_w values for all piglets are provided in Table 3.3. These k_w estimates were derived using individual τ_b values, except for piglet 6 for whom it was necessary to use the group average value. There were no statistically significant differences between the $\Delta M_{b_{50}}/\Delta M_{b_0}$ values for the sonicated and non-sonicated regions. Similarly there was no significant difference in the k_w values between the two sides.

The mean pixel SNR measurements from the FEAST and DW-ASL data sets are shown in Table 3.4. As expected, the SNR for the FEAST data were higher than for the DW-ASL data because the former were acquired with a shorter PLD and a smaller b-value.

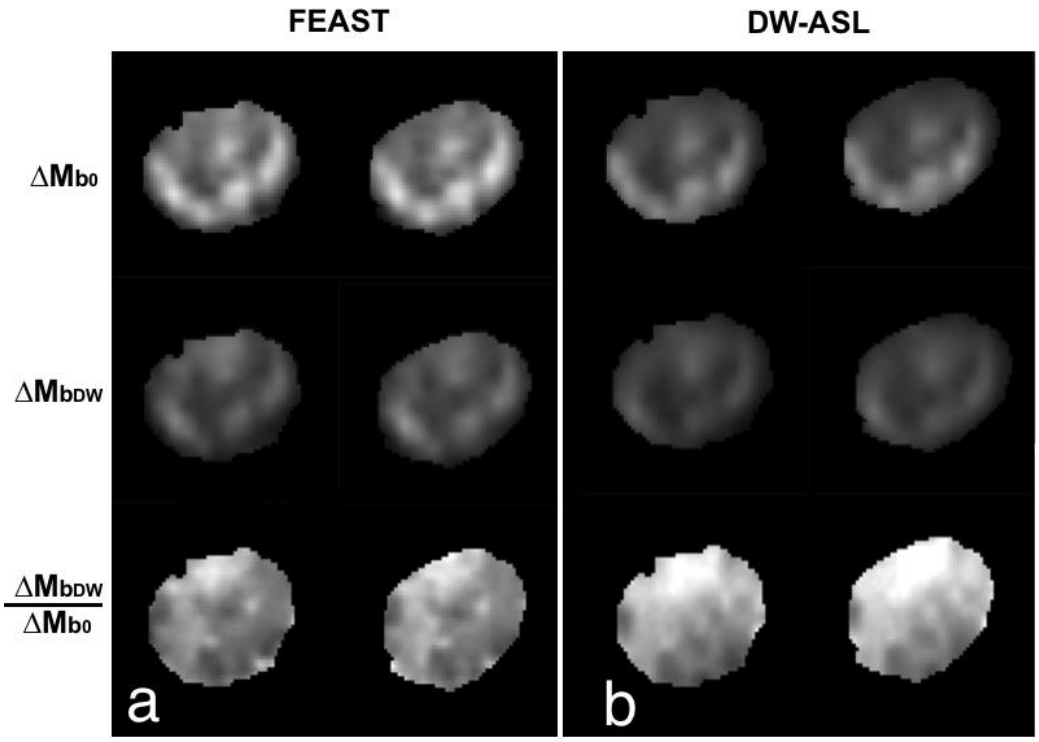

Figure 3.6: FEAST and DW-ASL data from one piglet: (a) FEAST data acquired with a PLD = 500 ms and (b) DW-ASL data acquired with a PLD = 1000 ms. Each data set shows the average diffusion-weighted ΔM_{b_0} in the first row and $\Delta M_{b_{DW}}$ in the second row. The ratio image, $\Delta M_{b_{DW}} / \Delta M_{b_0}$ is shown in the third row. The b values for FEAST and DW-ASL were 10 and 50 s/mm^2, respectively. All images have been first masked to show only the brain and smoothed with a 7-mm Gaussian filter.

Table 3.5: Calculated water exchange rate ($\boldsymbol{k_w}$) for the sonicated and non-sonicated regions for all 6 piglets.

Piglet	Sonicated		Non Sonicated	
	$\boldsymbol{Ratio}\frac{\Delta \boldsymbol{M_{b_{50}}}}{\Delta \boldsymbol{M_{b_0}}}$	$\boldsymbol{k_w}$ (min^{-1})	$\boldsymbol{Ratio}\frac{\Delta \boldsymbol{M_{b_{50}}}}{\Delta \boldsymbol{M_{b_0}}}$	$\boldsymbol{k_w}$ (min^{-1})
1	0.51	99	0.47	88
2	0.46	65	0.52	77
3	0.52	81	0.50	77
4	0.58	136	0.54	116
5	0.52	125	0.50	119
6	0.41	77	0.53	120
Mean	0.50 ± 0.06	97.17 ± 28.25	0.51± 0.02	99.50 ± 21.06

Table 3.7: Mean pixel SNR in the FEAST and DW-ASL image sets.

Image Series	SNR
FEAST ΔM_{b_0}	1.63 ± 0.41
FEAST $\Delta M_{b_{10}}$	0.83 ± 0.41
DW-ASL ΔM_{b_0}	1.07 ± 0.22
DW-ASL $\Delta M_{b_{50}}$	0.61 ± 0.15

Values were averaged across five piglets for FEAST and six piglets for DW-ASL.

Chapter 4

4 Discussion

The goal of this project was to assess if an ASL sequence designed to measure the rate of water exchange across the BBB would be sensitive to increases in BBB permeability (46). Focused ultrasound in combination with microbubbles was used to open the BBB in newborn piglets. As FUS has not been previously applied to this animal model, the first step was to optimize the FUS parameters using contrast-enhanced T_1-weighted MRI and Evans Blue dye to evaluate changes in permeability. Significant BBB opening was visualized in post Gd-DTPA T_1-weighted images for sonication powers greater than or equal to 2.5 W (0.97 MPa), as determined by comparing signal enhancement in the pre-defined sonicated region to a non-sonicated control region in the contralateral hemisphere. These results were also affirmed by the qualitative observations of EB dye leakage into the targetted region. At the highest power setting (6.0 W), there was evidence in the T_2^*-weighted images and the EB dye staining of intracerebral hemorrhaging, particularly near the ventricles. The sensitivity to bleeding is likely greater in this region because of an enhancement of the cavitational effect due to the difference in acoustic impedance between CSF and brain tissue (84).

There have been a few studies performing FUS on swine; however, these studies involved larger pigs, which required either a craniotomy or thinning of the skull to achieve a successful BBB disruption (84–86). Because of this, lower

overall peak negative pressures and shorter sonication times were required compared to the values used in this thesis. For example, Wei *et al*., observed an R_1 increase and EB dye enhancement in adult pigs with craniotomies at a FUS pressure of 0.43 MPa and hemorrhage at 0.56 MPa (85). Similarly, Liu *et al*., reported BBB disruption in pigs (5-8 kg) with thinned craniums at peak negative pressures of 0.52 and 0.78 MPa (86). Because the skull is substantially thinner in newborn piglets (approximately 1 to 2 mm in thickness), it was possible to sonicate through the intact head in the current study. However, the distortion caused by the skull, which we attempted to minimize by positioning the head normal to the ultrasound beam, would explain the higher power requirements. Previous studies have estimated that the beam distortion due to the skull can cause 30% to 50% loss in pressure (84,85). The power setting used in the current study was also greater than the value used in a rabbit model with the same FUS system. With rabbits, a power of 0.5 W for a sonication time of 120 s was sufficient to open the BBB, while power levels greater than 0.55 W resulted in hemorrhage (87).

In contrast to the Gd-DTPA T_1-weighted data, the $\Delta M_{b_{50}}/\Delta M_{b_0}$ ratio derived from the DW-ASL images showed no significant difference between the sonicated and non-sonicated ROIs. In fact, the difference between the mean values from the two ROIs was only 2% (Table 3.3). It was anticipated that the $\Delta M_{b_{50}}/\Delta M_{b_0}$ ratio would be greater in the sonicated region since an increase in BBB permeability would be expected to increase k_w, resulting in a greater fraction of labeled water diffusing the tissue compartment.

There are a number of reasons that could explain the apparent insensitivity of the DW-ASL technique to changes in BBB permeability. First, water exchange across the BBB could already be very fast and therefore opening the barrier would only cause a small increase in the amount of labeled water in the tissue compartment. To understand this relationship, the predicted capillary fraction of labeled water, A_1, is plotted as function of k_w in figure 4.1. This graph illustrates the non-linear relationship between A_1 and k_w and, more importantly, it demonstrates the small variation in A_1 at higher k_w values. For example, increasing k_w from 150 to 250 min^{-1} would only result in approximately a 25% change in A_1.

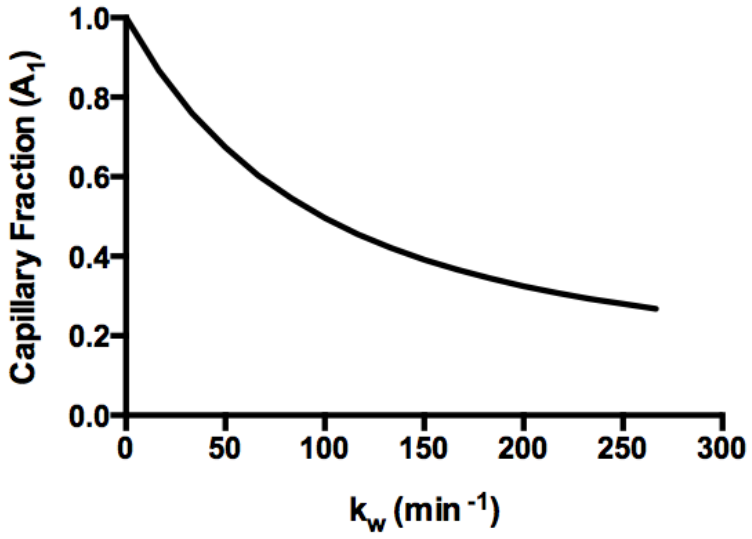

Figure 4.1: Predicted capillary fraction of labeled water (A_1) plotted as a function of the water-exchange rate (k_w). These simulated data were generated using T_{1b} = 1.26 s, T_{1a} = 1.49 s, a labeling duration of 1.5 s, τ_b = 1.06 s and a PLD of 1.0 s.

Higher k_w values could be expected considering that some studies have reported PS_w values greater than 300 ml/100 g/min (88,89), which would correspond to k_w values around 200 min^{-1} since the capillary blood volume is approximately 1.5 ml/100 g (90). However, there is considerable variation in PS_w estimates between studies, with values in the range of 120 to 150 mL/100 g/min reported for humans (88), monkeys (91) and rabbits (92). These estimates are in the range expected if k_w was closer to 100 min^{-1}, as measured in the current study. Furthermore, the predicted $\Delta M_{b_{50}}/\Delta M_{b_0}$ ratio for higher k_w values would be much greater than the values measured in this study. The average value was 0.53 ± 0.08, which indicates that only half of the labeled water diffused into the tissue.

A second possible reason why the DW-ASL sequence was unable to detect an increase in BBB permeability could be due to its inherently poor SNR. As shown in Table 3.4, the temporal SNR in a pixel was only around 1 in the DW-ASL images before applying the diffusion gradient and was reduced to 0.64 for b = 50 s/mm^2. The SNR limitations of ASL and the challenges it present for measuring k_w are known (41,47) and in the current study the number of repetitions, particularly for b = 50 s/mm^2, was chosen to overcome this limitation. Based on the number of repetitions acquired, the size of the sonicated ROI, and the pixel noise calculations, a change of 11 to 15% in $\Delta M_{b_{50}}/\Delta M_{b_0}$ should have been detectable in the current experiments. This prediction was confirmed by the reproducibility of the measured $\Delta M_{b_{50}}/\Delta M_{b_0}$ ratios given in Table 3.3. Based on

these data, a difference of 10.5% between the sonicated and non-sonicated regions would be significant for a sample size of 6.

A third possible reason that the DW-ASL sequence did not detect an increased in water exchange across the BBB may be that the applied diffusion gradient did not sufficiently suppress the signal from the labeled water in the capillary compartment. The strength of the diffusion gradient was selected based on the average speed of blood in capillaries (35). Although it was only applied in the one direction (slice encoding), the assumption is that the tortuosity of cerebral vessels is sufficient, such that vascular spins undergo pseudo random motion as they move through the capillaries. The adequacy of the selected diffusion gradient strength and any directional dependency could be explored by repeating the experiment across a range of b values and by applying diffusion gradients in all three directions. However, this would be extremely challenging with the current experiment considering the large number of repetitions required to detect changes in a focal spot caused by FUS sonication and the finite window that the BBB remains open (83). Since each targeted location requires a separate injection of microbubbles and a two-minute period of sonication, the total duration could quickly become prohibitively long. Future experiments could be conducted at higher field strengths to improve the SNR and with an animal species, such as the rat, in which whole-brain changes in permeability have been successively conducted using carotid infusion of mannitol (21,93,94).

Other parameters measured in this study include the tissue transit time (τ_b). Since k_w values are affected by transit times and signal contributions from

arterial blood, τ_b was measured using the FEAST approach with a PLD chosen that is greater than the arterial transit time. The PLD of 1 s applied during the DW-ASL sequence was slightly shorter than the measured τ_b of 1.06 s, indicating that not all of the labeled water reached the brain tissue. However, the $\Delta M_{b_{10}}/\Delta M_{b_0}$ ratio of 0.53 ± 0.13 calculated in this study was similar to the $\Delta M_{b_{10}}/\Delta M_{b_0}$ value of 0.57 recorded in the previous study on humans (47).

Chapter 5

5 Summary

5.1 Limitations and Future Work

The BBB in a piglet model was successfully opened by FUS as demonstrated by both contrast-enhanced MRI and Evans blue dye. Unfortunately, although the water exchange rate measured in this study was in good agreement to previous studies and had good reproducibility, the study failed to find any detectable increases in water permeability in the sonicated regions by DW-ASL. However, DW-ASL is only one approach for measuring water exchange across the BBB by MRI. Alternative techniques include the use of vascular contrast agents to alter the blood relaxation times, either the T_1 or the T_2 (44,95,96). A recent study conducted by Huang *et al*., reported a significant increase in their measured water exchange index (WEI) after a bolus injection of mannitol (95,96). Another ASL-based technique is to use differences in the relaxation times (T_1 and T_2) between blood and tissue, rather than diffusion gradients, to distinguish the fractions of labeled water in the two compartments. The sensitivity of this approach was recently improved by the development of a 3D gradient and spin echo PASL technique with a multi-echo readout (44,97). This method focused on T_2 imaging because of the greater difference between T_2 values in blood and tissue compared to T_1 differences. The increase in SNR by 3D imaging helps compensate for the subtle signal changes caused by relaxation differences (43,97). However, the greater sensitivity of this approach compared

to DW-ASL has not been tested. The advantage of a non-contrast-based method is it could be easily incorporated into on-going clinical studies, such as investigating changes in the BBB integrity associated with dementia. Newer techniques such as the above will improve the understanding of pathophysiological mechanisms of BBB associated with AD progression and would also assist in the discovery of new therapeutic treatment methods.

5.2 Conclusion

In conclusion, the water exchange rate is a challenging parameter to measure, in particular due to the extremely controlled nature of water transport across the BBB. This study demonstrated the ability to successfully open the BBB in a piglet model to create a BBB-compromised environment. The k_w and PS_w measurements were in good agreement with the previous studies, but lacked sensitivity to discern permeability changes between the sonicated and non-sonicated regions.

ASL still remains a non-invasive, safe and a quantitative technique for measuring perfusion, but further work is required to develop a method that is sensitive to water exchange.

References

1. Paulson OB. Blood – brain barrier, brain metabolism and cerebral blood flow. European Neuropsychopharmacology 2002; 12:495–501.

2. Li G, Yuan W, Fu BM. A model for the blood-brain barrier permeability to water and small solutes. Journal of Biomechanics 2010; 43:2133–2140.

3. Fisher M. Pericyte signaling in the neurovascular unit. Stroke 2009; 40:S13–S15.

4. Rubin LL, Staddon JM. The cell biology of the blood-brain barrier. Annual Review of Neuroscience [Internet] 1999; 22:11–28.

5. Stamatovic SM, Keep RF, Andjelkovic AV. Brain endothelial cell-cell junctions: how to “open” the blood brain barrier. Current Neuropharmacology 2008; 6:179–192.

6. Re F, Moresco R, Masserini M. Nanoparticles for neuroimaging. Journal of Physics D: Applied Physics 2012; 45:073001.

7. Bonomini F, Francesca B, Rezzani R. Aquaporin and Blood Brain Barrier. Current Neuropharmacology 2010; 8:92–96.

8. Papadopoulos MC, Verkman AS. Aquaporin-4 and Brain Edema. Pediatric Nephrology 2007; 22:778–84.

9. Weller RO, Subash M, Preston SD, Mazanti I, Carare RO. Perivascular Drainage of Amyloid-Beta Peptides from the Brain and Its Failure in Cerebral Amyloid Angiopathy and Alzheimer’s Disease. Brain pathology 2008;18:253–266.

10. Popescu BO, Toescu EC, Popescu LM, Bajenaru O, Muresanu DF, Schultzberg M, Bogdanovic N. Blood-Brain Barrier Alterations in Ageing and Dementia. Journal of the neurological sciences 2009; 283:99–106.

11. Zlokovic BV. The blood-Brain Barrier in Health and Chronic Neurodegenerative Disorders. Neuron 2008; 57:178–201.

12. Zlokovic BV. Neurovascular Pathways to Neurodegeneration in Alzheimer’s Disease and Other Disorders. Nature reviews: Neuroscience 2011; 12:723–738.

13. Farrall AJ, Wardlaw JM. Blood-brain barrier: ageing and microvascular disease--systematic review and meta-analysis. Neurobiology of Aging 2009; 30:337–352.

14. Abbott NJ. Inflammatory mediators and modulation of blood-brain barrier permeability. Cellular and Molecular Neurobiology 2000;20:131–147.

15. Bowman GL, Quinn JF. Alzheimer's disease and the Blood-Brain Barrier: Past, Present and Future. Aging Health 2008; 4:47–55.

16. Dysken MW, Nelson MJ, Hoover M, Kuskowski M, Mcgeachie R. Rapid Dynamic CT Scanning in Primary Degenerative Dementia and Age-Matched Controls. BIOL PSYCHIATRY 1990; 28:425–434.

17. Ujiie M, Dickstein DL, Carlow DA, Jefferies WA. Blood-brain barrier permeability precedes senile plaque formation in an Alzheimer disease model. Microcirculation 2003;10:463–470.

18. Starr JM, Farrall AJ, Armitage P, McGurn B, Wardlaw J. Blood-brain barrier permeability in Alzheimer's disease: a case-control MRI study. Psychiatry Research 2009; 171:232–241.

19. Bronge L, Wahlund LO. White matter lesions in dementia: an MRI study on blood-brain barrier dysfunction. Dement Geriatr Cogn Disord [Internet] 2000; 11:263–267.

20. Shindo H, Hanyu H, Shimizu S, Iwamoto T. Blood-brain barrier dysfunction in white matter lesions of elderly patients with dementia. Journal of Tokyo Medical University 2005; 63:395–400.

21. Silva AC, Zhang W, Williams DS, Koretsky AP. Estimation of water extraction fractions in rat brain using magnetic resonance measurement of perfusion with arterial spin labeling. Magnetic Resonance in Medicine 1997; 35:58–68.

22. Detre JA, Leigh JS, Williams DS, Koretsky AP. Perfusion imaging. Magnetic Resonance in Medicine 1992; 23:37–45.

23. St Lawrence KS, Frank JA, McLaughlin AC. Effect of restricted water exchange on cerebral blood flow values calculated with arterial spin tagging: a theoretical investigation. Magnetic Resonance in Medicine 2000; 44:440–449.

24. Liu TT, Brown GG. Measurement of cerebral perfusion with arterial spin labeling: Part 1. Methods. Journal of the International Neuropsychological Society 2007; 13:517–525.

25. Koziak AM, Winter J, Lee T-Y, Thompson RT, St Lawrence KS. Validation study of a pulsed arterial spin labeling technique by comparison to perfusion computed tomography. Magnetic Resonance Imaging 2008;26:543–553.

26. Xu G, Rowley HA, Wu G, Alsop DC, Shankaranarayanan A, Dowling M, Christian BT, Oakes TR, Johnson SC. Reliability and precision of pseudo-continuous arterial spin labeling perfusion MRI on 3.0 T and comparison with 15O-water PET in elderly subjects at risk for Alzheimer's disease. NMR in Biomedicine 2010;23:286–293.

27. Uchihashi Y, Hosoda K, Zimine I, et al. Comparison of CBF measurement by ASL and SPECT in Patients with Internal Carotid Artery Stenosis. In: Proc.Intl.Soc.Mag.Reson.Med. ; 2009. p. 34.

28. Wong EC, Buxton RB, Frank LR. Theoretical and Experimental Comparison of Continuous and Pulsed Arterial Spin Labeling Techniques for Quantitative Perfusion Imaging. Magnetic Resonance in Medicine 1998;40:348–355.

29. Williams DS, Detre JA, Leigh JS, Korestsky AP. Magnetic Resonance Imaging of Perfusion Using Spin Inversion of Arterial Water. Pro Natl Acad Sci. 1992;89:212–216.

30. St Lawrence KS, Owen D. Arterial Spin Labeling: A Magnetic Resonance Imaging Technique for Measuring Cerebral Perfusion. In: Stergios Stergiopoulos, editor. Advanced Signal Processing: Theory and Implementation for Sonar, Radar, and Non-Invasive Medical Diagnostic Systems. 2nd ed. CRC Press; 2009. pp. 653–685.

31. Alsop DC, Detre J a. Multisection cerebral blood flow MR imaging with continuous arterial spin labeling. Radiology. 1998; 208:410–416.

32. Detre JA, Alsop DC. Perfusion magnetic resonance imaging with continuous arterial spin labeling: methods and clinical applications in the central nervous system. European Journal of Radiology 1999; 30:115–124.

33. Wu W-C, Fernández-Seara M, Detre JA, Wehrli FW, Wang J. A theoretical and experimental investigation of the tagging efficiency of pseudocontinuous arterial spin labeling. Magnetic Resonance in Medicine 2007;58:1020–1027.

34. Dai W, Garcia D, de Bazelaire C, Alsop DC. Continuous flow-driven inversion for arterial spin labeling using pulsed radio frequency and gradient fields. Magnetic Resonance in Medicine 2008;60:1488–1497.

35. Wang J, Alsop DC, Song HK, Maldjian JA, Tang K, Salvucci AE, Detre JA. Arterial transit time imaging with flow encoding arterial spin tagging (FEAST). Magnetic Resonance in Medicine 2003; 50:599–607.

36. Wu W, St Lawrence KS, Licht DJ, Wang DJJ. Quantification Issues in Arterial Spin Labeling Perfusion. Top Magn Reson Imaging 2010; 21:65–73.

37. Parkes LM, Tofts PS. Improved accuracy of human cerebral blood perfusion measurements using arterial spin labeling: Accounting for capillary water permeability. Magnetic Resonance in Medicine 2002;48:27–41.

38. Zhou J, Wilson DA, Ulatowski JA, Traystman RJ, van Zijl PC. Two-compartment exchange model for perfusion quantification using arterial spin tagging. Journal of Cerebral Blood Flow and Metabolism 2001; 21:440–455.

39. Li K, Zhu X, Hylton N, Jahng G-H, Weiner MW, Schuff N. Four-phase single-capillary stepwise model for kinetics in arterial spin labeling MRI. Magnetic Resonance in Medicine 2005; 53:511–518.

40. Hales PW, Phipps KP, Kaur R, Clark CA. A two-stage model for in vivo assessment of brain tumor perfusion and abnormal vascular structure using arterial spin labeling. PloS one 2013;8:e75717.

41. Carr JP, Buckley DL, Tessier J, Parker GJM. What levels of precision are achievable for quantification of perfusion and capillary permeability surface area product using ASL? Magnetic Resonance in Medicine 2007; 58:281–289.

42. St Lawrence KS, Wang J. Effects of the apparent transverse relaxation time on cerebral blood flow measurements obtained by arterial spin labeling. Magnetic Resonance in Medicine 2005; 53:425–433.

43. Günther M, Oshio K, Feinberg DA. Single-shot 3D imaging techniques improve arterial spin labeling perfusion measurements. Magnetic Resonance in Medicine 2005; 54:491–498.

44. Gregori J, Schuff N, Kern R, Günther M. T2-based arterial spin labeling measurements of blood to tissue water transfer in human brain. Journal of Magnetic Resonance Imaging 2013; 37:332–342.

45. Silva AC, Williams DS, Koretsky AP. Evidence for the exchange of arterial spin-labeled water with tissue water in rat brain from diffusion-sensitized measurements of perfusion. Magnetic Resonance in Medicine 1997; 38:232–237.

46. Wang J, Fernández-Seara MA, Wang S, St Lawrence KS. When perfusion meets diffusion: in vivo measurement of water permeability in human brain. Journal of Cerebral Blood Flow and Metabolism 2007; 27:839–849.

47. St Lawrence KS, Owen D, Wang DJJ. A two-stage approach for measuring vascular water exchange and arterial transit time by diffusion-weighted perfusion MRI. Magnetic Resonance in Medicine 2011;67:1275–1284.

48. Doolittle ND, Abrey LE, Ferrari N, et al. Targeted Delivery in Primary and Metastatic Brain Tumors : Summary Report of the Seventh Annual Meeting of the Blood-Brain Barrier Disruption Consortium Targeted Delivery in Primary and Metastatic Brain Tumors : Summary Report of the Seventh Annual Meetin. Clin Cancer Res 2002; 8:1702–1709.

49. Doolittle ND, Miner ME, Hall WA, et al. Safety and efficacy of a multicenter study using intraarterial chemotherapy in conjunction with osmotic opening of the blood-brain barrier for the treatment of patients with malignant brain tumors. Cancer 2000; 88:637–647.

50. Ergin A, Wang M, Zhang J, Bigio I, Joshi S. Noninvasive in vivo optical assessment of blood brain barrier permeability and brain tissue drug deposition in rabbits. Journal of Biomedical Optics 2012;17:057008.

51. Marchi N, Teng Q, Nguyen MT, Franic L, Desai NK, Masaryk T, Rasmussen P, Trasciatti S, Janigro D. Multimodal investigations of trans-endothelial cell trafficking under condition of disrupted blood-brain barrier integrity. BMC neuroscience 2010;11:34.

52. Rebeles F, Fink J, Anzai Y, Maravilla KR. Blood-brain barrier imaging and therapeutic potentials. Top Magn Reson Imaging 2006;17:107–116.

53. Lynn J, Zwemer R, Chick A, Miller A. A New Method for the Generation and Use of Focused Ultrasound in Experimental Biology. J Gen Physiol 1942;26:179–193.

54. Park E-J, Zhang Y-Z, Vykhodtseva N, McDannold N. Ultrasound-mediated blood-brain/blood-tumor barrier disruption improves outcomes with trastuzumab in a breast cancer brain metastasis model. Journal of Controlled Release 2012;163:277–284.

55. Zippel DB, Frcs MZP. The Use of MR Imaging Guided Focused Ultrasound in Breast Cancer Patients; a Preliminary Phase One Study and Review. Breast Cancer 2005;12:32–38.

56. Gianfelice D, Khiat A, Amara M, Belblidia A, Boulanger Y. MR imaging-guided focused ultrasound surgery of breast cancer: correlation of dynamic contrast-enhanced MRI with histopathologic findings. Breast Cancer Research and Treatment 2003;82:93–101.

57. Liberman B, Gianfelice D, Inbar Y, et al. Pain palliation in patients with bone metastases using MR-guided focused ultrasound surgery: a multicenter study. Annals of Surgical Oncology 2009;16:140–146.

58. Gianfelice D, Gupta C, Kucharczyk W, Bret P, Havill D, Clemons M. Palliative Treatment of Painful Bone Metastases with MR Imaging – guided Focused Ultrasound. Radiology 2008;249:355–363.

59. Crouzet S, Rebillard X, Chevallier D, Rischmann P, Pasticier G, Garcia G, Rouviere O, Chapelon J-Y, Gelet A. Multicentric oncologic outcomes of high-intensity focused

ultrasound for localized prostate cancer in 803 patients. European Urology 2010;58:559–66.

60. Crouzet S, Murat FJ, Pasticier G, Cassier P, Chapelon JY, Gelet A. High intensity focused ultrasound (HIFU) for prostate cancer: current clinical status, outcomes and future perspectives. International Journal of Hyperthermia 2010;26:796–803.

61. Fegoun ABE, Barret E, Prapotnich D, Soon S, Cathelineau X, Rozet F, Galiano M, Sanchez-salas R, Vallancien G. Focal Therapy with High-Intensity Focused Ultrasound for Prostate Cancer in the Elderly . A Feasibility Study with 10 Years Follow-Up. Clinical Urology 2011;37:213–222.

62. Vykhodtseva N, McDannold N, Hynynen K. Progress and problems in the application of focused ultrasound for blood-brain barrier disruption. Ultrasonics 2008;48:279–296.

63. Hynynen K, Mcdannold N, Vykhodtseva N, Jolesz FA. Noninvasive MR Imaging-guided Focal Opening of the Blood-Brain Barrier in Rabbits. Radiology 2001;220:640–646.

64. Hynynen K, McDannold N. Chapter V: MRI-Guided Focused Ultrasound for Local Tissue Ablation and other Image-Guided Interventions. Emerging Therapeutic Ultrasound. In: Wu J, Nyborg W, editors. 5 Toh Tuck Link, Singapore 596224: World Scientific Publishing Co.Pte.Ltd; 2006. pp. 167–201.

65. Samiotaki G, Vlachos F, Tung Y-S, Konofagou EE. A quantitative pressure and microbubble-size dependence study of focused ultrasound-induced blood-brain barrier opening reversibility in vivo using MRI. Magnetic Resonance in Medicine 2012;67:769–777.

66. Konofagou EE. Optimization of the ultrasound-induced blood-brain barrier opening. Theranostics 2012;2:1223–1237.

67. Vykhodtseva N, Sorrentino V, Jolesz F, Bronson R, Hynynen K. MRI Detection of the Thermal Effects of Focused Ultrasound on the Brain. Ultrasound in Med & Biol 2000;26:871–880.

68. Tung Y-S, Vlachos F, Choi JJ, Deffieux T, Selert K, Konofagou EE. In vivo transcranial cavitation threshold detection during ultrasound-induced blood-brain barrier opening in mice. Physics in Medicine and Biology 2010;55:6141–55.

69. Stapleton S, Goodman H, Zhou Y-Q, Cherin E, Henkelman RM, Burns PN, Foster FS. Acoustic and Kinetic Behaviour of Definity in Mice Exposed to High Frequency Ultrasound. Ultrasound in Medicine & Biology 2009;35:296–307.

70. Caskey CF, Stieger SM, Qin S, Dayton PA, Ferrara KW. Direct observations of ultrasound microbubble contrast agent interaction with the microvessel wall. The Journal of the Acoustical Society of America 2007;122:1191–1200.

71. McDannold N, Vykhodtseva N, Hynynen K. Blood-brain barrier disruption induced by focused ultrasound and circulating preformed microbubbles appears to be characterized by the mechanical index. Ultrasound in medicine & biology 2008;34:834–840.

72. Yang F-Y, Fu W-M, Yang R-S, Liou H-C, Kang K-H, Lin W-L. Quantitative evaluation of focused ultrasound with a contrast agent on blood-brain barrier disruption. Ultrasound in Medicine & Biology 2007;33:1421–1427.

73. Yang F-Y, Fu W-M, Chen W-S, Yeh W-L, Lin W-L. Quantitative evaluation of the use of microbubbles with transcranial focused ultrasound on blood-brain-barrier disruption. Ultrasonics Sonochemistry 2008;15:636–643.

74. Weng J-C, Wu S-K, Yang F-Y, Lin W-L, Tseng W-YI. Pulse sequence and timing of contrast-enhanced MRI for assessing blood-brain barrier disruption after transcranial focused ultrasound in the presence of hemorrhage. Journal of Magnetic Resonance Imaging 2010;31:1323–1330.

75. Chopra R, Vykhodtseva N, Hynynen K. Influence of exposure time and pressure amplitude on blood-brain-barrier opening using transcranial ultrasound exposures. ACS Chemical Neuroscience 2010;1:391–398.

76. O'Reilly MA, Waspe AC, Ganguly M, Hynynen K. Focused-ultrasound disruption of the blood-brain barrier using closely-timed short pulses: influence of sonication parameters and injection rate. Ultrasound in Med & Biol 2011;37:587–594.

77. O'Reilly MA, Hynynen K. A PVDF receiver for ultrasound monitoring of transcranial focused ultrasound therapy. IEEE transactions on Biomedical Engineering 2010;57:2286–2294.

78. O'Reilly MA. Methods for Focused Ultrasound-Induced Blood-Brain Barrier Disruption: Error Reduction and Active Control. University of Eastern Finland Library / Sales of publications P.O. Box 107, FI-80101 Joensuu, Finland tel. +358-50-3058396 http://www.uef.fi/kirjasto; 2012 p. 147.

79. Deffieux T, Konofagou EE. Numerical Study of a Simple Transcranial Focused Ultrasound System Applied to Blood-Brain Barrier Opening. IEEE Transactions of Ultrasonics, Ferroelectrics, and Frequency Control 2010;57.

80. Song J, Pulkkinen A, Huang Y, Hynynen K. Investigation of Standing-Wave Formation in a Human Skull for a Clinical Prototype of a Ultrasound (MRgFUS) Phased Array : An Experimental and Simulation Study. IEEE Transactions of Biomedical Engineering 2012;59:435–444.

81. Itani M, Mattrey RF. The effect of inhaled gases on ultrasound contrast agent longevity in vivo. Molecular Imaging and Biology 2011;14:40–46.

82. Mullin, L., Gessner, R., Kwan J., Kaya, M., Borden, MA, Dayton P. Effect of Anesthesia Carrier Gas on In-Vivo Circulation Times of Ultrasound Microbubble Contrast Agents in Rats. Contrast Med Mol Imaging 2011;6:126–131.

83. Xie F, Boska MD, Lof J, Uberti MG, Tsutsui JM, Porter TR. Effects of transcranial ultrasound and intravenous microbubbles on blood brain barrier permeability in a large animal model. Ultrasound in Med & Biol 2008;34:2028–2034.

84. Liu H-L, Chen P-Y, Yang H-W, et al. In vivo MR quantification of superparamagnetic iron oxide nanoparticle leakage during low-frequency-ultrasound-induced blood-brain barrier opening in swine. Journal of Magnetic Resonance Imaging 2011;34:1313–1324.

85. Wei K, Tsai H, Lu Y, Yang H, Hua M, Wu M, Chen P, Huang C, Yen T, Liu H. Neuronavigat ion-Guided Focused Ultrasound Induced Blood-Brain Barrier Opening : A Preliminary Study in Swine. American Society of Neuroradiology 2012:1–5.

86. Liu H-L, Jan C-K, Chu P-C, Hong J-C, Lee P-Y, Hsu J-D, Lin C-C, Huang C-Y, Chen P, Wei K-C. Design and Experimental Evaluation of a 256-Channel Dual-Frequency Ultrasound Phased-Array System for Transcranial Blood – Brain Barrier Opening and Brain Drug Delivery. IEEE Transactions of Biomedical Engineering 2014;61:1350–1360.

87. Ahmed H, Waspe AC, Chopra R, Hynynen K, Lee T-Y. Focused Ultrasound Induced Blood-Brain-Barrier Disruption : Quantitative Evaluation using Dynamic Contrast Enhanced-Computed Tomography. In: RSNA 2012 : Scientific Formal (Paper) Presentations. ; 2012.

88. Herscovitch P, Raichle ME, Kilbourn MR, Welch MJ. Positron emission tomographic measurement of cerebral blood flow and permeability-surface area product of water using [15O]water and [11C]butanol. Journal of Cerebral Blood Flow and Metabolism 1987;7:527–542.

89. Schwarzbauer C, Morrissey SP, Deichmann R, Hillenbrand C, Syha J, Adolf H, Nöth U, Haase A. Quantitative magnetic resonance imaging of capillary water permeability and regional blood volume with an intravascular MR contrast agent. Magnetic Resonance in Medicine 37:769–777.

90. Pawlik G, Rackl A, Bing RJ. Quantitative Capillary Topography and Blood Flow in the Cerebral Cortex of Cats: An In Vivo Microscopic Study. Brain Research 1981;208:35–58.

91. Eichling JO, Raichle ME, Grubb Jr RL, Ter-Pogossian MM. Evidence of the Limitations of Water as a Freely Diffusible Tracer in Brain of the Rhesus Monkey. Circulation Research 1974;35:358–364.

92. St. Lawrence KS, Lee T-Y. An Adiabatic Approximation to the Tissue Homogeneity Model for Water Exchange in the Brain: II. Experimental Validation. Journal of Cerebral Blood Flow and Metabolism 1998;18:1378–1385.

93. Tanaka Y, Nagaoka T, Nair G, Ohno K, Duong TQ. Arterial spin labeling and dynamic susceptibility contrast CBF MRI in postischemic hyperperfusion, hypercapnia, and after mannitol injection. Journal of Cerebral Blood Flow and Metabolism 2011;31:1403–1411.

94. Martin J, Maris A, Ehtesham M, Singer R. Rat Model of Blood-Brain Barrier Disruption to Allow Targeted Neurovascular Therapeutics. Journal of Visualized Experiments 2012;69:e50019.

95. Caravan P, Kim YR, Sorenson A. System and Method for Determining Blood- Brain Barrier Permeability to Water. 2012.

96. Huang S, Farrar CT, Dai G, Kwon SJ, Bogdanov A a, Rosen BR, Kim YR. Dynamic monitoring of blood-brain barrier integrity using water exchange index (WEI) during mannitol and CO_2 challenges in mouse brain. NMR in Biomedicine 2012:376–385.

97. Feinberg DA, Günther M. Cerebral Blood Flow Imaging with 3D GRASE ASL Sequence Increases SNR and Shortens Acquisition Time. MAGNETOM Flash 2009;3:62–69.

.

Appendices

Appendix A – Animal Protocols

Appendix A: Animal Protocol 1 – 2011/2012

From:
Sent: Tuesday, December 20, 2011 12:20 PM
To:
Cc:
Subject: eSirius Notification - New Animal Use Protocol is APPROVED2011-063::1

Western

AUP Number: 2011-063
PI Name: St. Lawrence, Keith
AUP Title: Assessment Of The Sensitivity Of A Non-contrast Magnetic Resonance Imaging Technique To Changes In Blood-brain Barrier Permeability.

Official Notice of Animal Use Subcommittee (AUS) Approval: Your new Animal Use Protocol (AUP) entitled "Assessment Of The Sensitivity Of A Non-contrast Magnetic Resonance Imaging Technique To Changes In Blood-brain Barrier Permeability." has been APPROVED by the Animal Use Subcommittee of the University Council on Animal Care. This approval, although valid for four years, and is subject to annual Protocol Renewal.2011-063::1

1. This AUP number must be indicated when ordering animals for this project.
2. Animals for other projects may not be ordered under this AUP number.
3. Purchases of animals other than through this system must be cleared through the ACVS office. Health certificates will be required.

The holder of this Animal Use Protocol is responsible to ensure that all associated safety components (biosafety, radiation safety, general laboratory safety) comply with institutional safety standards and have received all necessary approvals. Please consult directly with your institutional safety officers.

Submitted by: Copeman, Laura
on behalf of the Animal Use Subcommittee
University Council on Animal Care

The University *of* Western Ontario
Animal Use Subcommittee / University Council on Animal Care
Health Sciences Centre, ● London, Ontario ● CANADA – N6A 5C1
PH: 519-661-2111 ext. 86768 ● FL 519-661-2028
Email: auspc@uwo.ca ● http://www.uwo.ca/animal/website/

Appendix A: Animal Protocol 2 – 2012/2013

From:
Sent: Monday, January 28, 2013 10:15 AM
To:
Cc:
Subject: eSirius Notification - Annual Protocol Renewal APPROVED by the AUS 2011-063::1

Western

2011-063::1:

AUP Number: 2011-063
AUP Title: Assessment of the sensitivity of a non-contrast magnetic resonance imaging technique to changes in blood-brain barrier permeability.
Yearly Renewal Date: 01/01/2013

The YEARLY RENEWAL to Animal Use Protocol (AUP) 2011-063 has been approved, and will be approved for one year following the above review date.

1. **This AUP number must be indicated when ordering animals for this project.**
2. **Animals for other projects may not be ordered under this AUP number.**
3. **Purchases of animals other than through this system must be cleared through the ACVS office. Health certificates will be required.**

REQUIREMENTS/COMMENTS
Please ensure that individual(s) performing procedures on live animals, as described in this protocol, are familiar with the contents of this document.

The holder of this Animal Use Protocol is responsible to ensure that all associated safety components (biosafety, radiation safety, general laboratory safety) comply with institutional safety standards and have received all necessary approvals. Please consult directly with your institutional safety officers.

Submitted by: Kinchlea, Will D
on behalf of the Animal Use Subcommittee

Curriculum Vitae

Appendix A: Animal Protocol 3 – 2013/2014

From:
Sent: January 9, 2014 1:37 PM
To:
Cc:
Subject: eSirius Notification - Annual Protocol Renewal APPROVED by the AUS 2011-063::2

Western

2011-063::2:

AUP Number: 2011-063
AUP Title: Assessment of the sensitivity of a non-contrast magnetic resonance imaging technique to changes in blood-brain barrier permeability.
Yearly Renewal Date: 01/01/2014

The YEARLY RENEWAL to Animal Use Protocol (AUP) 2011-063 has been approved, and will be approved for one year following the above review date.

1. This AUP number must be indicated when ordering animals for this project.
2. Animals for other projects may not be ordered under this AUP number.
3. Purchases of animals other than through this system must be cleared through the ACVS office. Health certificates will be required.

REQUIREMENTS/COMMENTS
Please ensure that individual(s) performing procedures on live animals, as described in this protocol, are familiar with the contents of this document.

The holder of this Animal Use Protocol is responsible to ensure that all associated safety components (biosafety, radiation safety, general laboratory safety) comply with institutional safety standards and have received all necessary approvals. Please consult directly with your institutional safety officers.

Submitted by: Savage, Colleen
on behalf of the Animal Use Subcommittee

Curriculum Vitae

Name: Harini Pandithasekera

Post-secondary Education and Degrees:

Western University
London, Ontario, Canada
2011 Sept - Present
M.Sc Medical Biophysics.

Ryerson University
Toronto, Ontario, Canada
2006 Sept - 2011 April
B.Sc Medical Physics Co-Operative.

Honours and Awards:

Western Graduate Research Scholarship (WGRS)
2011 - 2013

Deans List, Ryerson University
2010 - 2011

Related Work Experience

Research Assistant / Graduate Student
Lawson Health Research Institute, London, Ontario, Canada
2011 Sept - Present
Supervisor: Dr. Keith St. Lawrence

Research Assistant
Ryerson University, Toronto, Ontario, Canada
2010 Sept - 2011 July
Supervisor: Dr. Jahan Tavakkoli

Undergraduate Research Intern
Applied Modern Physics Group – P21
Los Alamos National Laboratory, Los Alamos, NM, USA
2009 June - 2010 Apr
Supervisor: Dr. Michelle Espy

Science Tutor
Learning Success Center
Ryerson University, Toronto, Ontario, Canada
2008 Sept - 2008 Dec

Posters:

- Pandithasekera H, Ahmed H, Hadway J, Butler J, Lee T-Y, St. Lawrence, K, “Optimization of Focused Ultrasound Parameters for Disrupting the Blood-Brain Barrier in Piglets”, London Health Research day. London, ON Canada (March 2013).

- Pandithasekera H and Tavakkoli J, “Sonophoresis: Application of Low Intensity Therapeutic Ultrasound for Transdermal Topical Drug Delivery”, Undergraduate Thesis Presentations. Department of Physics. Ryerson University, Toronto, Canada (April 2011).

- Pandithasekera H and Espy M, “MagViz- an Application of Ultra Low-Field MRI: Characterization and Stability”, Los Alamos National Laboratory – 9th Annual Student symposium “Championing Scientific Careers”, Los Alamos, NM, USA (August 2009)

Talks:

- Nath P, Pandithasekera H, Araya Y, Espy M, “ A Tunable Permanent Magnet circuit for Magnetophoresis”, XXV Congress of the International Society for the Advancement of Cytometry, Seattle, WA, USA (May 2010).